SveBeFo

STIFTELSEN SVENSK BERGTEKNISK FORSKNING
OCH SVENSKA BERGMEKANIKGRUPPEN
SWEDISH ROCK ENGINEERING RESEARCH
AND SWEDISH NATIONAL GROUP ISRM

SVENSKA BIDRAG TILL ISRM:s ELFTE INTERNATIONELLA BERGMEKANIKKONGRESS

LISSABON 2007

SveBeFo Rapport 85

STIFTELSEN SVENSK BERGTEKNISK FORSKNING
OCH SVENSKA BERGMEKANIKGRUPPEN
SWEDISH ROCK ENGINEERING RESEARCH
AND SWEDISH NATIONAL GROUP ISRM

SVENSKA BIDRAG TILL ISRM:s ELFTE INTERNATIONELLA BERGMEKANIKKONGRESS LISSABON 2007

Swedish Contributions to 11th International Congress on Rock Mechanics Lisbon 2007

Reprinted from the 11th ISRM Congress Proceedings held
9 – 13 July 2007 in Lisbon, Portugal, "**The Second Half Century of Rock Mechanics"**

Stockholm 2007
ISSN 1104 – 1773
ISRN SVEBEFO-R—85—SE

CONTENTS Page

Fluid flow and tracer transport simulations for rock fractures under normal loading and shear displacement

T. Koyama & L. Jing
Department of Land and Water Resources Engineering, Royal Institute of Technology (KTH), Sweden

ABSTRACT: The fluid flow and tracer transport in rock fractures during shear processes has been an important issue in rock mechanics and is investigated in this paper using Finite Element Method (FEM) for fluid flow and particle tracking simulations, considering evolutions of aperture, transmissivity and flow rate, with large shear displacements under different normal stress and stiffness conditions as measured during laboratory coupled shear-flow tests. Flow and tracer transport results shows that more realistic flow and transport phenomena/mechanism were captured due to more proper treatment of contact areas compared with pervious works reported in the literatures.

1 INTRODUCTION

Coupled stress-flow-tracer transport processes in rock fractures are increasingly important research topics for high-level radioactive waste disposal facilities in crystalline rocks because their safety assessments are mainly based on the knowledge of paths and travel times of radioactive nuclide transport that is dominated by groundwater flow in rock fractures.

As far as laboratory tests for rough rock fractures are concerned, laboratory studies focusing on the effect of both normal and shear stresses on fluid flow through rock fractures, so-called coupled shear-flow tests, have been a particular attraction due to its importance to understand and quantify the coupled stress-flow processes in fractured rocks (e.g. Esaki *et al*., 1999; Auradou *et al*., 2005). The coupled shear-flow tests have been performed not only under constant normal stress/load (CNL) condition but also constant normal stiffness (CNS) condition recently (Li *et al*., 2006a, b). However, no coupled shear-flow-tracer tests have been performed under combined normal stress and shear displacement even the effect of the shear on the transport phenomena has been investigated without considering normal stresses (Plouraboue *et al*., 2000).

Fluid flow and solute transport simulations in rough fractures are often performed without considering effects of any stresses, normal stress without any shear displacement (Thompson, 1991; Jeong and Song, 2005) or shear displacement without normal stress (Koyama *et al*., 2006a). The Reynolds equation is commonly applied to simulate such tests instead of the Navier-Stokes equation. How to measure or calculate the fracture aperture under different normal stresses and shear displacements during the coupled stress-flow tests and numerical simulations for such tests are the most essential points to understand the processes, interpret the testing and simulation results and quantify the hydraulic properties. The important phenomenon of shear induced anisotropy and heterogeneity of aperture distribution and its effects on fluid flow and transport in fractures, such as the more significant flow in the direction perpendicular to the shear, was reported in Koyama *et al*. (2006a, b). These findings represent an important step for more physically meaningful understanding of the coupled shear-flow-transport processes in rock fractures.

In the present study, laboratory shear-flow tests for fracture replicas under different normal stresses and normal stiffness conditions were simulated by using numerical simulations with FEM considering simulated evolutions of aperture and transmissivity with large shear displacements first. Next, the unidirectional flow perpendicular to the direction of shear, which is difficult to be realized in the laboratory shear-flow tests, was predicted. Finally, particle movement in the fracture during shear was simulated using streamline particle tracking method. The distributions of fracture aperture and its evolution during shearing and the flow rate were calculated from the initial aperture and shear dilations and compared with results measured in the laboratory coupled shear-flow tests. The contact areas in the fractures were treated correctly with zero aperture values with a special algorism so that more realistic flow velocity fields and particle transport paths were captured.

2 EXPERIMENTAL STUDY

2.1 *Sample preparation*

A natural rock fracture surface, labeled J3, were taken from the construction site of Omaru power plant in Miyazaki prefecture in Japan and used as the parent fracture surface in this study. Three replicas of fracture specimens were manufactured, named as J3-1, J3-2 and J3-3, with the J3 as the parent fracture surface. The specimens are 100 mm in width, 200 mm in length and 100 mm in height, respectively. They were made of mixtures of plaster, water and retardant with weight ratios of 1: 0.2: 0.005. The surfaces of the natural rock fractures were firstly re-cast by using resin, and then the two parts of a fracture specimen were manufactured based on the resin replica. By doing so, the two parts of each fracture specimens used in this study

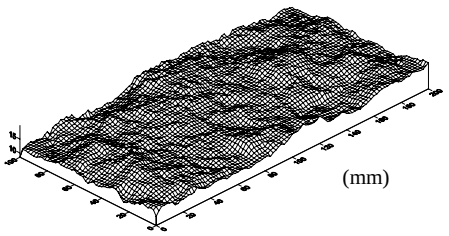

Figure 1. 3-D models of fracture specimen J3 based on the measured topographical data.

are almost perfectly mated as the initial contact ratio very close to 1.0. A 3-D laser scanning profilometer system was employed to obtain the topographical data of rock fracture surface J3, generating a scanning grid with a scanning interval of 0.2 mm in both *x* and *y*-axes, as shown in Fig. 1 (Li *et al*., 2006a, b).

2.2 *Laboratory shear-flow tests*

A series of coupled shear-flow tests under CNL and CNS conditions (a constant normal stress of 1.0 MPa for J3-1, normal stiffness of 0.2 GPa/m with an initial normal stress of 1.0 MPa for J3-2 and normal stiffness of 0.5 GPa/m with an initial stiffness of 1.0 MPa for J3-3, respectively) were carried out using the newly developed apparatus in Nagasaki University, Nagasaki, Japan. The details about features of the coupled shear-flow testing apparatus and testing procedure were reported in Li *et al*. (2006a, b).

2.3 *Aperture calculation during shear*

The mean aperture of each scanned grid zone was calculated at each shear displacement interval (1.0 mm) based on the initial aperture and shear dilations measured in the laboratory tests. Numerical shearing is simulated by moving the upper surface by a horizontal translation of 1.0 mm in the shear direction, then uplifting by the dilation increment according to the measured mean shear dilation value at that shear interval. Shear displacement was applied up to 18 mm. Since initial aperture is zero for fully mated specimens, full contact is assumed everywhere with zero aperture as the initial condition in the numerical simulations. When a grid zone has its two opposing surfaces separated, it represents a void zone and its aperture is evaluated as the mean distance in the direction normal to the mean plane of the fracture. When a grid zone's two opposing surfaces are just in touch or penetrate each other with negative values of contact distance, it represents a contact zone and is assigned with a zero aperture. In reality the latter represents surface damage/asperity degradation.

3 NUMERICAL SIMULATION

3.1 *Governing equations*

The fluid flow was simulated using the commercial FEM software, COMSOL Multiphysics that solves the Reynolds equation for steady state flow with full saturation of the sample. The evolutions of the aperture distributions during the shearing were determined in each shearing step and the evolutions of the fracture transmissivity fields were calculated by assuming the local validity of the cubic law (Koyama *et al*., 2006a, b). In the numerical modeling of fluid flow, effect of gorge materials is ignored since negligible amount of gorge materials were observed during tests. Asperity deformation was not considered but damage at contact points were partially approximated by removing the overlapping parts of contacting asperities in the contact elements.

A Lagrangian approach for a particle tracking method was adopted for particle transport simulations, considering only the advection process. The random dispersion due to diffusion of the solute particles within the pore fluid, and other retardation mechanisms such as sorption or decay, were not taken into account. As steady-state fluid flow was under consideration, particle tracking along the streamlines was used (Koyama *et al*., 2006a).

3.2 *Boundary conditions and the treatment of contact area*

Both unidirectional flows parallel with and perpendicular to the shear direction were considered in the flow simulations by fixing the initial hydraulic heads of 0.1 m and 0 m along the left- and right-hand boundaries for the flow parallel with the shear direction (Fig. 2a), and the bottom and top boundaries for the flow perpendicular to the shear direction (Fig. 2b), respectively. The flow boundary condition for the flow parallel with the shear direction is the same as the one used in the laboratory coupled shear-flow tests. Since the sizes of the upper and lower parts of the specimens are the same, the actual contact lengths decrease during shear. As a result, the hydraulic gradient was not constant (became progressively larger) during shear.

In this study, contact areas/elements were numerically eliminated from the calculation domain and their boundaries were treated as additional internal boundaries with a zero flux condition $\partial h/\partial n \equiv (\nabla h)\cdot \mathbf{n} = 0$, where $\mathbf{n}$ is the outward unit normal vector, in order to satisfy conditions of no flow into or out of the contact areas (Zimmerman *et al.*, 1992), as shown in Fig. 2c.

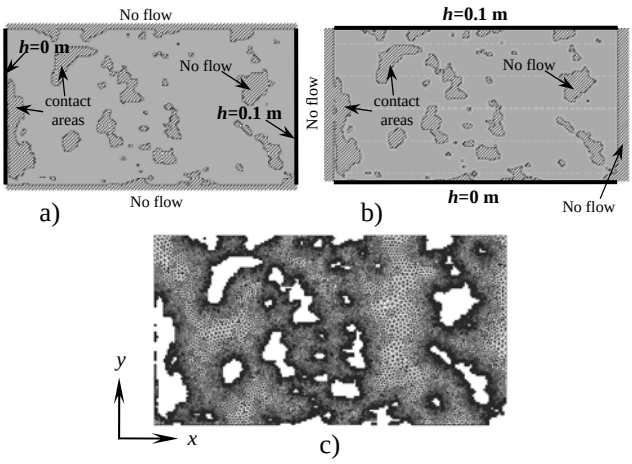

Figure 2. Boundary conditions for the flow a) parallel with and b) perpendicular to the shear displacement, and c) calculation mesh.

4 RESULTS

4.1 *Numerical simulation of the laboratory shear-flow tests*

The simulated results of flow velocities are superimposed in Fig. 3, with transmissivity evolutions during shear at different shear displacements for fracture J3 under constant normal stress of 1 MPa, J3-1. Since the samples were assumed to be fully mated with a zero initial aperture, no flow is possible at the start. At 1 mm of shear displacement, the contact areas are widely and uniformly distributed over the whole fracture sample. More continuous flow paths start to form at 2 mm of shear displacements, and continue to grow into main flow paths with continued decrease of contact areas and increase of transmissivity, with increasing shear displacement The shear caused widely distributed contact areas and complicated void space geometry, leading to complex structure of transmissivity and flow velocity fields. As a result, flow patterns (or stream lines) become very tortuous. This phenomenon is the well-known 'channelling effect'.

The flow rate at the outlet boundary (along x=0) of sample J3 with different normal loading conditions were compared between laboratory tests and numerical simulations as shown in Fig. 4. The general behaviors of the simulated flow rate variations with shear displacements under different normal stress/stiffness conditions were captured for all three conditions of normal loading, agree well with measured results. Both simulated and measured flow rates show the sharp increase at about 2 mm shear

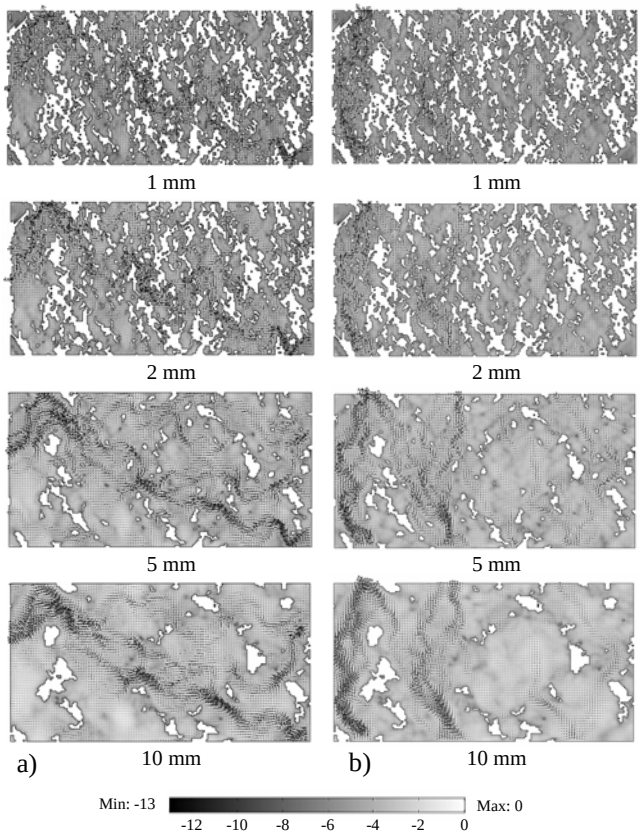

Figure 3. Flow velocity fields with transmissivity evolutions for J3-1 (under 1 MPa of normal stress), for the flow a) parallel with and b) perpendicular to the shear displacement.

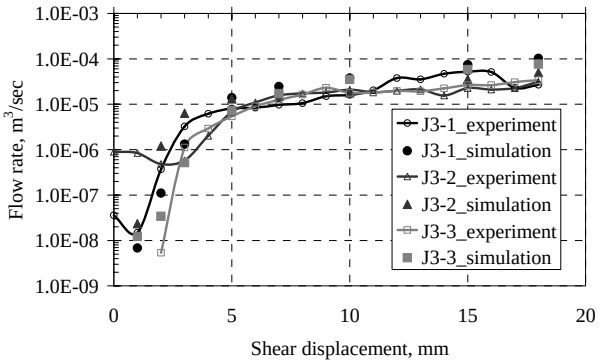

Figure 4. Comparison of the flow rate at the outlet between laboratory experiment and numerical prediction for fracture sample J3 under different normal loading conditions J3-1, J3-2 and J3-3.

displacements and continue to increase but with a progressive reduction of gradient, and more stabilized flow rate after the 5 mm shear displacement. The general increase of flow rate is about 4-5 orders of magnitude from the initial state before shear.

4.2 *Simulation for shear-induced flow anisotropy*

In Fig. 3, the simulated results of flow velocity fields are also compared between in the direction parallel with (Fig. 3a) and perpendicular to (Fig. 3b) the shear displacement. Figure 5 shows the flow rates calculated at two cross sections. One is the flow rate in x-direction at position of x=0 and the other is the flow rate in y-direction at position y=0.1m. It should be noted that the flow rates are normalized by dividing hydraulic gradient and edge length of the fracture samples since the samples are not square (the edge length is different) and therefore hydraulic gradient are different. The two sets of result show completely different flow patterns. When the general flow direction is parallel to the shear direction (Fig. 3a), the flow is more tortuous. When the general flow direction is perpendicular to the shear direction (Fig. 3b), the flow field becomes more regular through higher transmissivity channels, with larger

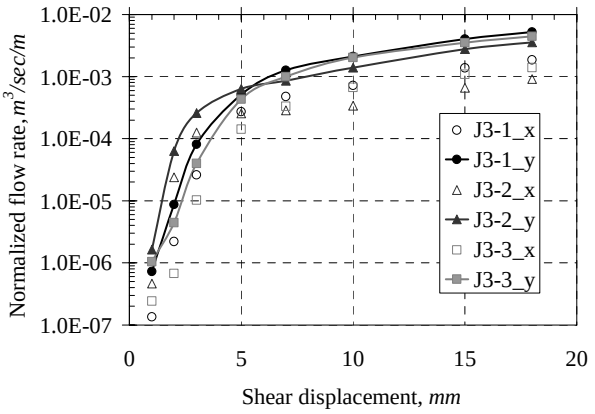

Figure 5. Comparison of the normalized flow rates at the outlet for fracture sample J3 under different normal loading conditions, J3-1, J3-2 and J3-3, between the flows in the direction parallel with (x-direction) and perpendicular to (y-direction) the shear.

flow rate than that with flow parallel with shear, about from 5 to 10 times, with increasing shear displacement.

4.3 *Particle tracking*

The particle movements for sample J3 under a normal stress of 1.0 MPa, J3-1 were predicted. The results of the particle motion are shown in Fig. 6, considering only flow parallel with shear, with 100 particles were evenly distributed at the inlet initially. Figure 7 shows the breakthrough curves at different shear displacements. From these figures, particles started coming out of the sample after 3 mm shear displacement and some of the particles stay inside the fracture due to the local flow rotations caused by the zero-aperture contact areas (Fig. 6). Starting at 5 mm shear displacement, the most of the particles travel much faster and therefore the breakthrough curves become steeper. This means that fracture dispersivity becomes lower and advective transport is more dominant. In addition, after 5 mm shear displacement, the shape of the breakthrough curves does not change very much, due to the more steady state of particle paths as indicated in Figs. 3 and Fig. 6.

5 CONCLUSIONS

The general fluid flow and particle transport behaviors presented here are more realistic, due to more proper treatment of contact areas with zero aperture in flow and particle transport simulations, compared with earlier results reported in literature about flow simulations without stress or shear, and with artificially assigned very small aperture values for the contact areas to avoid singularities of FEM models caused by such non-zero aperture in contact areas.

This result clearly illustrates the limitations of the traditional boundary conditions in shear-flow tests in which the significant effect of shear dilation on flow in the direction perpendicular to shear direction cannot be captured and therefore is often neglected. This shortcoming may lead to significant underestimation of the fluid transmissivity of the rock fractures during shearing processes

At present only numerical simulations can illustrate

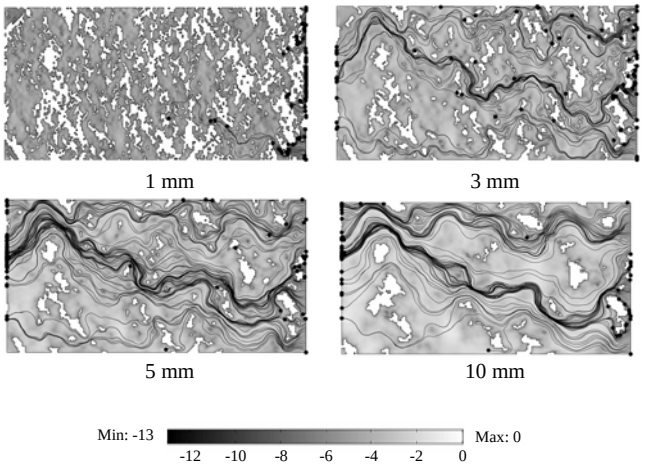

Figure 6. Particle movements for the flow parallel with the shear displacement under normal stress of 1MPa.

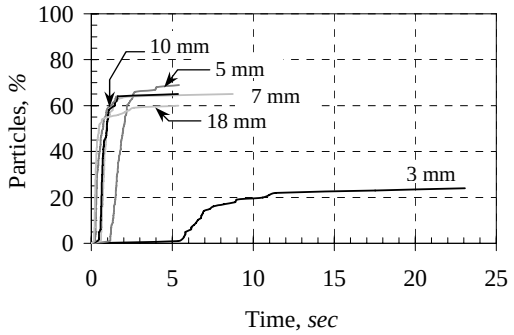

Figure 7. Breakthrough curves at different shear displacements for sample J3 under normal loading condition J3-1.

realistically the process of complex evolution of the flow localization (channeling) and its effect on the tracer transport during shear under different normal loading conditions, since direct measurement and visualization is impossible.

ACKNOWLEDGEMENT

The authors thank Dr. Y. Jiang's group at Nagasaki University, Japan for supplying the experimental data.

REFERENCES

Auradou, H., Drazer, G., Hulin, J.P. and Koplik, J. 2005. Permeaqbility anisotropy induced by the shear displacement of rough fracture walls. *Water Resour Res*, 41, W09423, doi: 10.1029/2005WR 003938.

Esaki, T., Du, S., Mitani, Y., Ikusada, K. and Jing, L. 1999. Development of a shear-flow test apparatus and determination of coupled properties for a single rock joint. *Int J Rock Mech Min Sci*, 36: 641-50.

Jeong, W. and Song, J. 2005. Numerical investigations for flow and transport in a rough fracture with hydromechanical effect. *Energy Sources*, 27: 997-1011.

Koyama, T., Vilarrassa, V., Neretnieks I. and Jing, L. 2006a Shear-induced flow channels in a single rock fracture and their effect on particle transport, Manuscript submitted to *Water Resour Res*, March, 2006.

Koyama, T., Fardin, N., Jing, L. and Stephansson, O. 2006b. Numerical simulation of shear induced flow anisotropy and scale dependent aperture and transmissivity evolutions of fracture replicas. *Int J Rock Mech Min Sci*, 43(1): 89-106.

Li, B., Jiang, Y., Koyama, T., Jing, L. and Tanabashi, Y. 2006a. Experimental study on hydro-mechanical behaviour of rock joints by using parallel-plates model containing contact area and artificial fractures. Manuscript submitted to *Int J Rock Mech Min Sci*, October, 2006.

Li, B., Jiang, Y., Saho, R., Tasaku, Y. and Tanabashi, Y. 2006b. An investigation of hydromechanical behaviour and transportability of rock joints. In: *Rock Mechanics in Underground Construction*, eds. Leung CF Y and Zhou YX, World Scientific, pp. 321.

Plouraboue, F., Kurowski, P., Boffa, J. M., Hulin, J. P. and Roux, S. 2000. Experimental study of the transport properties of rough self-affine fractures. *J Contam Hydrol*, 46: 295-318.

Thompson, M.E. 1991. Numerical simulation of solute transport in rough fractures. *J Geophys Res*, 96(B3): 4157-4166.

Zimmerman, R.W., Chen, D.W. and Cook, N.G.W. 1992. The effect of contact area on the permeability of fractures. *J Hydrology*, 139: 79-96.

Measurement of micro crack volume in low porosity crystalline rock

L. Jacobsson & M. Flansbjer
Building Technology and Mechanics, SP Technical Research Institute of Sweden, Borås, Sweden

R. Christiansson
Swedish Nuclear Fuel and Waste Management CO, Stockholm, Sweden

T. Jansson
Tyrens AB, Gothenburg, Sweden

ABSTRACT: The in-situ porosity is used for modelling diffusion within crystalline rock in order to determine its retention properties. Such information is important for the safety analysis when siting a deep geological repository for nuclear waste. The total porosity is determined in the laboratory on drill core specimens, which have experienced stress relaxation causing an opening of natural pores and stress-induced microcracks. The in-situ porosity can be estimated by subtracting the porosity due to microcracks from the total porosity determined in laboratory. Hydrostatic compression tests on granite specimens from two sites, with loading up to 50 MPa and 100 MPa, were carried out in order to determine the microcrack volume. The tests indicated that major closure of microcracks had occurred at 50 MPa. Moreover, the in-situ porosity was found to be approximately 10-15 % less than the total porosity in the laboratory samples studied.

1 INTRODUCTION

The Swedish Nuclear and Fuel Waste Management CO (SKB) is currently carrying out investigations at two candidate sites (Forsmark and Oskarshamn) for a final repository for nuclear spent fuel, which include extensive surface and borehole investigations down to a maximum depth of 1000 m, and site modelling involving different geoscientific disciplines. The results are used for preliminary Design Studies and Safety Assessments. Among the activities, investigations and modeling of the transport properties of the bedrock are carried out to develop site-specific descriptions of the radionuclide transport processes. The investigations yield parameters used for the radionuclide transport calculations performed by Safety Assessment in models developed by Safety Assessment and others (SKB 2005, 2006).

The transport properties of the rock mass depend on porosity, diffusion and sorption. Porosity is measured on cores. The diffusivity is quantified via the formation factor which is obtained from diffusion experiments and electrical resistivity measurements. The resistivity can be measured in laboratory on rock samples saturated with NaCl and in borehole in-situ experiments (Löfgren & Neretnieks 2003).

In-situ measurements of the formation factor at depth for the Forsmark site indicate a considerably lower value than corresponding values from laboratory measurements (SKB 2005). Furthermore, the laboratory resistivity measurements suggest an increasing formation factor with depth while no such increase could be observed for the in-situ results. This discrepancy between the laboratory and in-situ formation factor could be related to an increase in the porosity of the laboratory samples caused by stress release. This notion is supported by a tendency for sonic velocities measured on cores from the Forsmark site to decrease below approximately 500-550 m depth (SKB 2005). It is known that extracting core samples at depth can lead to a significant increase in crack porosity (Chernis 1984, Martin & Stimpson 1994) and the dependence of stress on the formation factor was investigated by Skagius & Neretnieks (1986). In this paper we report the porosity measurements on laboratory samples from various depths and compare to the estimated in-situ porosity.

2 OCCURRENCE OF MICROCRACKS

In crystalline rocks the porosity occurs from two sources: (1) new stress-induced microcracks from the coring process, and (2) naturally closed pores that open when the in-situ stress is released. In hard rocks natural pores tend to have polygonal shapes, while stress-induced microcracks tend to have long-parallel walls, see Figure 1. Investigations of granite by SKB (2005) and SKB (2006) yielded values of the natural porosity between 0.1-0.4%. Chernis & Robertson (1987) found that most grain boundary cracks form around quartz grains in a laboratory study of microcracks on Lac du Bonnet granite. Ninety percent of natural cracks occur along grain boundaries. The remaining cracks that could be distinguished from stress-relief cracks occur as intragranular cracks, chiefly in feldspars.

There is a stress limit for which stress-induced microcracking occurs in a drilled core. Stress redistribution

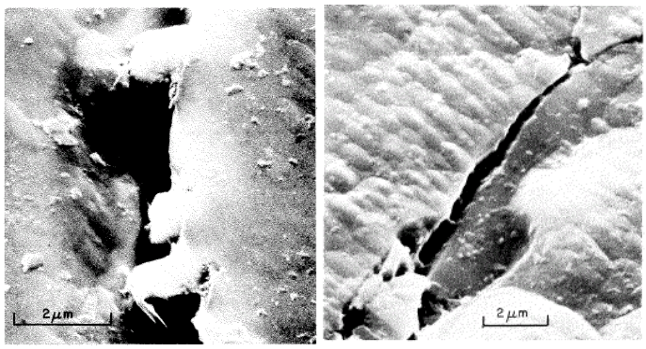

Figure 1. Pore structure in Lac du Bonnet granite, from Chernis (1984). The left photo is a natural pore while the right photo is a stress-induced microcrack.

takes place in the specimen around the coring bit while coring, which may or may not exceed the threshold for inducing new microcracks (Lim et al. 2007). The larger the amount of stress release, the greater the potential for an increase in pore volume due to stress-induced cracks.

Walsh (1965) found that the required pressure to fully close a penny-shaped crack or pore within a solid material subjected to hydrostatic compression was

$$p_c = \pi E\alpha/4\,(1 - \nu^2), \quad (1)$$

where E is Young's modulus, ν is the Poisson ratio and α is the ratio of the width to the length of the crack. Hence, the crack closing pressure p_c is expected to be lower for stress-induced cracks, which are long and thin, than for natural pores, which are significantly shorter and wider, cf. Figure 1.

The natural distribution of α for pores and microcracks in a rock material yields a response curve, which is initially mainly associated with closure of microcracks, yielding a non-linear progressively increasing bulk stiffness. The non-linearity vanishes when the cracks are closed even though a slight non-linearity associated with closing of pores above some pressure level may be observed, cf. Figure 2. Zero porosity will yield a linear response entirely given by the intact particles constituting the grain structure, while an increase of porosity will lead to an increased volumetric deformation. Results from hydrostatic compression tests on low porous rock in the literature are reported by, cf. Stephens (1964), Brace (1965), Simmons & Siegfried (1974) and Siegfried & Simmons (1978).

3 SPECIMEN AND TEST DESCRIPTION

The specimens tested originate from drill hole KFM01A (subsequently denoted FM) at the Forsmark site investigation area and drill hole KLX17A (subsequently denoted LX) at the Oskarshamn site investigation area. The specimens were saturated by water. The core diameters were 51 and 50 mm, respectively. The Forsmark specimens of medium-grained granite have a clear foliatiated texture, cf. Figure 3. The Oskarshamn specimens of Ävrö granite are uniform. Both granites have an average grain size of 3-4 mm. Porosity measurements were carried out on neigbouring specimens.

Six strain gauges placed at mid-height were used on each specimen. Three were oriented axially, denoted AV, BV and CV and three circumferential, denoted AH, BH and CH, allowing measurements of possible anisotropic response,

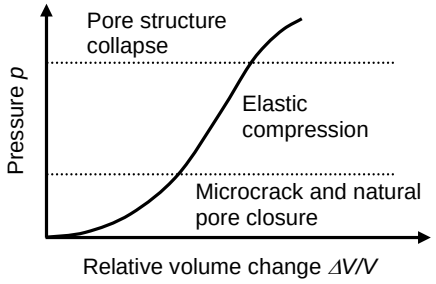

Figure 2. Schematic response during a hydrostatic compression test. Pessure vs. volumetric deformation, cf. Goodman (1989).

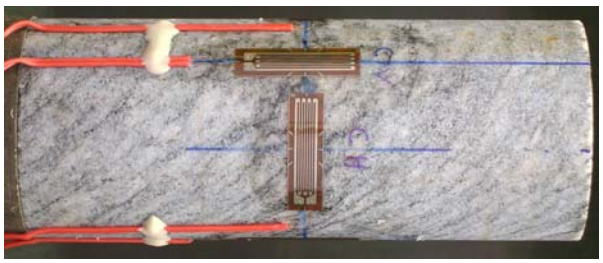

Figure 3. Lay-out of strain gauges. Specimen FM-25, from the Forsmark site. Notice the foliations.

see Figure 3. A gauge length of 20 mm was used in order to capture a somewhat homogenized response with respect to the grain structure and microcrack distribution.

The test machine is equipped with a pressure vessel and a computer controlled pressure intensifier. The strain gauges were connected to Wheatstone bridges using a two wire coupling plus a third wire, a sense channel, was connected to the point right before the wires were going in the cell. This connection implies compensation for any temperature changes and cable resistances in the circuit up to the electrical connector on the cell wall. The Wheatstone bridge circuits were connected to high accuracy amplifier modules of two types, HBM ML38 and ML10B. The data acquisition device was a HBM MGCplus unit. The strain gauge channels were calibrated using a shunt resistance.

A number of pitfalls concerning the usage of foil strain gauges relevant for the current type of test set-up exist, such as varying lateral pressure sensitivity, scatter due to varying bonding layer thickness and bonding problems on porous and curved material surfaces (Brace 1964, Hoffman 1989). Acrylic adhesive was reported by Lau & Chandler (2004) to work in order to install strain gauges on wet rock specimens and was therefore chosen. A method to properly install the strain gauges and to protect them for moisture was devised.

Uniaxial and hydrostatic compression tests were carried out on aluminium specimens prior to the tests on rock specimens in order to check the experimental set-up and quantify the measurement error, which was found to be within 40 microstrain (0.004%) at a hydrostatic pressure of 50 MPa. The magnitude of the scatter was linearly proportional to the applied pressure.

The specimen was placed inside the pressure cell between platens and sealed using a thin rubber membrane. Oil surrounded the specimen except under the lower platen as the platen was fixed to the cell bottom. This set-up yields an isotropic loading. Tests with two different load sequences were conducted. Type 1: Loading from 0.1-50 MPa, hold at 50 MPa for 15 minutes and unload 50-0.1 MPa and hold for 15 minutes. Type 2: Loading from 0.1-50 MPa, hold at 50 MPa for 5 minutes, loading from 50-100 MPa, hold for 5 minutes, unload 100-50 MPa, short hold time, and unload 50-0.1 MPa and hold for 5 minutes. The pressure rate was 10 MPa/min during both loading and unloading, except for one test (LX-8) in which it was 2 MPa/min.

4 RESULTS

The results from the hydrostatic compression tests are shown in Figures 4-5. The volumetric strain ε_{vol} was computed as $\varepsilon_{vol} = \varepsilon_a + 2\varepsilon_r$, where $\varepsilon_a = (\varepsilon_{AV} + \varepsilon_{BV} + \varepsilon_{CV}) / 3$

and $\varepsilon_r = \varepsilon_\varphi = (\varepsilon_{AH} + \varepsilon_{BH} + \varepsilon_{CH}) / 3$. The tangent bulk compliance, defined as $\beta = d\varepsilon_{vol} / dp$, were evaluated both at initial loading (β_{ini}) and at 50 MPa (β_{max}) at the unloading curve in order to illustrate the amount of non-linearity and to obtain a comparable indicator for major closure of microcracks by comparing the values of β_{max}.

The microcrack volume strain is computed as, cf. Walsh (1965), $\varepsilon_{MC} = \varepsilon_{vol,max} - \beta_{max} p_{max}$, where $\varepsilon_{vol,max}$ and p_{max} refer to values at 50 MPa. The measured material response displays an anisotropic behaviour. The specimen anisotropy and inhomogenity is quantified, given in percent, according to $\Psi = 3 \times (\varepsilon_{max} - \varepsilon_{min}) / \varepsilon_{vol,max} \times 100$, where ε_{min} and ε_{max} refer to the minimum and the maximum strain value in any of the strain gauges at the fully compressed state after the hold time. Moreover, the anisotropy between the axial and the circumferential directions at the fully compressed state after the hold time, given in percent, has been defined as $\Psi_{HV} = 3 \times (\varepsilon_{r,max} - \varepsilon_{a,max}) / \varepsilon_{vol,max} \times 100$, where $\varepsilon_{a,max} = \max(\varepsilon_a)$ and $\varepsilon_{r,max} = \max(\varepsilon_r)$. The parameter results from all tests are summarized in Table 1.

The bulk compliances β_{ini} and β_{max} have been plotted versus depth (Figure 6). The values of β_{max} are between 18.4 and 20.0 (10^{-3} GPa^{-1}) except for the specimens at 223 m depth from Oskarshamn. Brace (1965) reports corresponding values to β_{max} of 19.1 and 19.9 (10^{-3} GPa^{-1}) for two specimens of different types of granite. This validates the current measurements. Moreover, due to the similar values of β_{max} it may be concluded that a cell pressure of 50 MPa was sufficient for this type of rock to close the majority of the microcracks.

It can be noted that the difference between β_{ini} and β_{max} seems to increase with depth indicating increased non-linearity and growing crack porosity. Figure 7 (also Table 1) confirms a growing crack volume with depth. It is also evident by the results that the total crack volume is larger in samples from the Forsmark site, as ε_{MC} = 0.035-0.078% for the Forsmark specimens and ε_{MC} = 0.011-0.048% for the Oskarshamn specimens. Moreover, by studying Ψ_{HV}, cf. Table 1, which is greater than or equal zero (except for one specimen), one may assume that a larger part of the micro cracks probably are oriented along, or with a small angle to, the core axis direction This is more pronounced in the Forsmark specimens, which may be coupled to the foliated structure, cf. Figure 3.

5 DISCUSSION AND CONCLUDING REMARKS

The measurements using strain gauges seem to properly capture the response as the results are comparable to measurements on granite by Brace (1965), despite the known difficulties by using strain gauges subjected to lateral pressure. As mentioned before, the majority of microcracks seem to be closed at 50 MPa pressure. A hysteresis can be observed during the tests. Moreover, some creep deformation could be seen at full loading during the hold time. The hysteresis was less and almost no creep deformation could be observed in the test of 2 MPa/min. The creep rate rapidly decreases during the hold time at full loading during the 10 MPa/min-tests. This fact together with no significant difference between the values of β_{max} suggests that the results from the tests with loading rate of 10 MPa/min will yield similar results of the microcrack volume as tests conducted with a lower rate.

The horizontal in-situ stress magnitudes are generally higher at the Forsmark site compared to the Laxemar site (Martin & Christiansson, 2007). The major horizontal stress at Forsmark is in the range of 40-45 MPa while at Laxemar it is in the range of 22-25 MPa at 500 m depth. Based on the test results it appears that the crack volume in the core samples is dependent on in-situ stress magnitude, and thus the amount of stress relaxation. Especially the higher crack volume strain from samples taken below 500 m depth at

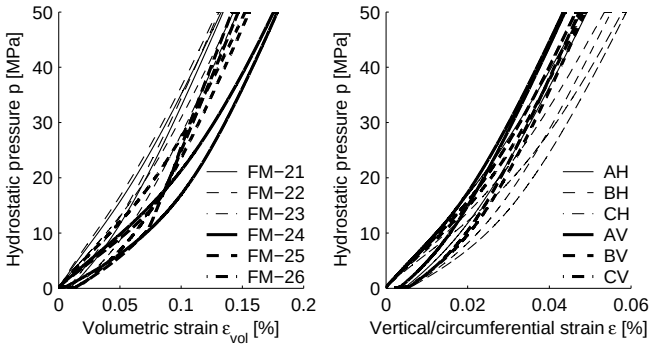

Figure 4. Results from Forsmark specimens. Left: Confining pressure vs. volumetric strain; Right: Confining pressure vs. strains from the individual gauges on specimen FM-26.

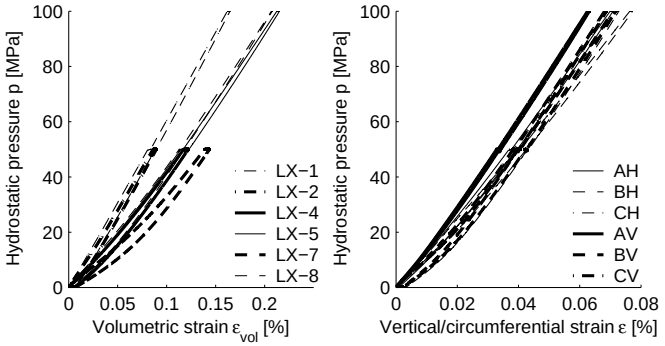

Figure 5. Results from Oskarshamn specimens. Left: Confining pressure vs. volumetric strain; Right: Confining pressure vs. strains from the individual gauges on specimen LX-5.

Table 1. Summary of hydrostatic compression test results.

Sample ID	Depth (m)	Porosity Φ (%)	Micro crack vol ε_{MC} (%)	Anisotropy Ψ (%)	Anisotropy Ψ_{HV} (%)	Bulk compliance (10^{-3} GPa^{-1}) β_{ini}	Bulk compliance (10^{-3} GPa^{-1}) β_{max}
FM-21	232	0.36	0.037	33	18	31.9	19.5
FM-22	233	0.36	0.035	21	9	29.8	19.2
FM-23	490	0.28	0.046	24	15	37.7	20.0
FM-24	490	0.28	0.078	37	15	51.0	20.0
FM-25	686	0.30	0.054	10	6	54.1	18.4
FM-26	686	0.30	0.057	29	15	40.2	19.7
LX-1	223	0.18	0.011	32	15	16.6	15.4
LX-2	223	0.18	0.013	16	-4	18.8	15.4
LX-4	382	0.34	0.028	19	9	26.6	19.0
LX-5	382	0.34	0.027	23	7	25.8	18.9
LX-7	556	0.36	0.048	20	0	32.3	19.2
LX-8	556	0.36	0.027	12	7	23.5	18.2

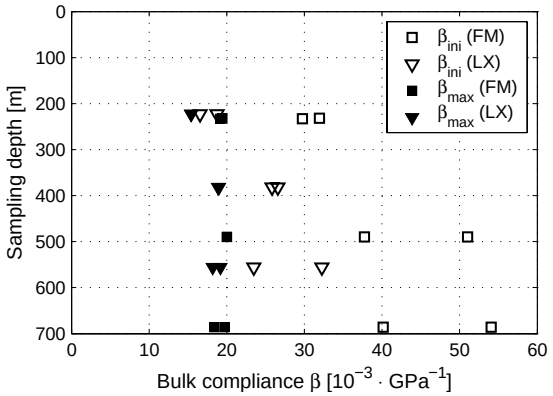

Figure 6. Bulk compliances vs. depth at initial (open symbols) and 50 MPa loading (solid symbols).

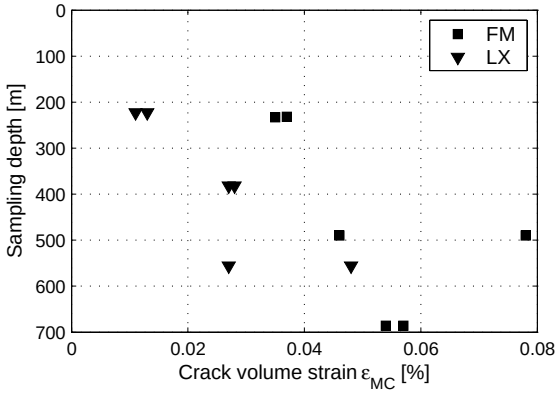

Figure 7. Crack volume vs. depth for all tests.

Forsmark (Figure 7) is in keeping with other information on stress-induced damage in core samples. Our findings also suggest that when the in-situ stress magnitudes are relatively low, the porosity of the core samples is dominated by the natural pores and the difference between the in-situ porosity and the core sample porosity is small. This is in keeping with the results from Löfgren & Neretnieks (2003) who found no significant difference between in-situ and laboratory measurements from a borehole at the Laxemar site, except when the core samples were within a geologically heterogeneous section. It seems that a certain difference in crack volume between laboratory specimens and rock in-situ is needed for the method to be able to detect a change of formation factor. With this finding in mind, it would mean that a crack volume strain (ε_{MC}) of at least 0.040 – 0.045% is needed in order to notice a change of the formation factor between the in-situ and laboratory measurements for the actual rock types.

The resistivity is dependent on how much and how far the formation water can penetrate into the rock. One possible explanation for which no change of the resistivity can be detected for small values of ε_{MC} could be that the uncertainty with the method such as accuracy and scatter requires a minimum resistivity change. Another hypothesis could be that there is a non-linear relation between how far into the rock the formation water can penetrate and the size of ε_{MC}. To elaborate on this, small values of ε_{MC} could be associated with damage from drilling and some stress release, yielding relatively short microcracks. With increasing stress release, the number of microcracks does not change, but the length of microcracks increase with a non-linear relation to the stress release. It should be pointed out that further investigations would be needed to clarify the underlying facts.

This study will be followed up by microscopic studies of the occurrence and distribution of pores and cracks to enhance our understanding of the nature of stress-induced core damage.

REFERENCES

Brace, W.F. 1964. Effect of pressure on electric resistance strain gages. *Exp. Mech.* 4:212-216.

Brace, W.F. 1965. Some new measurements of linear compressibility of rocks. *J. Geophys. Res.* 70(2):391-398.

Chernis, P.J. 1984. Comparison of the pore-microcrack structure of shallow and deep samples of the Lac du Bonnet granite. *Atomic Energy of Canada Limited, Technical Record TR-223.*

Chemis, P.J. & Robertson, P.B. 1987, Natural and stress-relief microcracks in the Lac Du Bonnet granite. In Katsube, T.J. and Hume, J.P. (eds.)*, Geotechnical studies at Whiteshell Research Area, Canada Centre for Min. Eng. Tech. Min. Res. Lab. Div., Report MRL 87-52 (INT).*

Goodman, R.E. 1989. *Introduction to rock mechanics, 2nd Ed*. Wiley.

Hoffman, K. 1989. *An introduction to measurements using strain gages*. Darmstadt : Hottinger Baldwin Messtechnik GmbH.

Lau, J.S.O. & Chandler, N.S. 2004. Innovative laboratory testing. *Int. J. Rock. Mech. Min. Sci.* 41:1427-1445.

Lim, S.S., Martin, C.D. & Christiansson, R. 2007. In-situ stress estimation using crack closure energy in crystalline rock. *In proceedings of 1st Canada-U.S. Rock Mechanics Symposium, Vancouver, May 2007.*

Löfgren, M. & Neretnieks I. 2003. Formation factor logging by electrical methods - Comparison of formation factor logs obtained in situ and in the laboratory. *Journal of Contaminant Hydrology 61: 107–115.*

Martin C.D. & Chrisitiansson R. 2007. Interpreting in-situ stress measurements using geological models. *In proceedings of ISRM 11th International Congress on Rock Mechanics*

Martin, C.D. & Stimpson, B. 1994. The effect of sample disturbance on laboratory properties of Lac du Bonnet granite. *Canadian Geotechnical Journal* 31: 692-702.

Siegfied, R.W. & Simmons, G. 1978. Characterization of oriented cracks with differential strain analysis. *J. Geophys. Res.* 83(B3):1269-1278.

Simmons, G., Siegfied, R.W. & Feves, M. 1974. Differential strain analysis: A new method for examining cracks in rocks. *J. Geophys. Res.* 79(29):4383-4385.

Skagius, K. & Neretnieks, I. 1986. Diffusivity measurements and electrical resistivity measurements in rock samples under mechanical stress. *Water Resources Research* 22(4):570-580.

SKB 2005. Preliminary Site Description. Forsmark area – version 1.2. *SKB Report R-05-18. Svensk Kärnbränslehantering AB, Stockholm, Sweden*.

SKB 2006. Site descriptive modeling. Forsmark stage 2.1. *SKB Report R-06-38. Svensk Kärnbränslehantering AB, Stockholm, Sweden.*

Stephens, D.R. 1964. The hydrostatic compression eight rocks. *J. Geophys. Res.* 69(14):2967-2978.

Walsh, J.B. 1965. The effect of cracks on the compressibility of rock. *J. Geophys. Res.* 70(2):381-389.

Propagation of large, twinned fractures in shear – a numerical investigation

Hossein Hakami
Itasca Geomekanik AB, Stockholm, Sweden

ABSTRACT: Large isolated fractures may happen to occur aligned or roughly so, separated by a portion of the host rock often called a rock bridge. Depending on how failure is defined, a bridge as such may fail as a result of the change in the state of *in situ* stress. Distinct Element program, 3DEC, was used to study the behaviour of the system "fracture-bridge-fracture". Fractures in question were circular in shape and were conditioned to propagate past their periphery, also into the rock bridge. Clearly the size of a bridge is decisive whether or not it fails. However, even if a bridge did not fail ; it remained mechanically intact; the excessive loading would lead to the interconnectivity of the fractures, separated by a bridge, from a geohydrological standpoint.

1 INTRODUCTION

A familiar two-dimensional picture from mapping of an exposed surface of a rock mass at different scales almost always shows a number of finite rock fractures together with presumably intact rock parties in between, see, e.g., Shen (1993). When groups of finite fractures tend to be aligned or nearly so, the segments of intact rock that separate the fractures are often called rock bridges. How intact rock bridges are is a matter of definition. In reality they are less intact than what one believes. This is simply because there exist quite a number of minor fractures that are hidden, and a conventional surface mapping cannot reveal those. In a real three-dimensional situation it may be somehow difficult to describe the geometry of a rock bridge and therefore major simplifications would normally be needed in a numerical study incorporating a rock bridge.

The fracture mechanics of the system "fracture – bridge – fracture" has been investigated by a number of investigators; see for example Petit & Barquins (1988) and Shen, (1993). In the context of repository design for final storage of radioactive waste, a question that arises in relation to the safety of a canister hole may tentatively be formulated as follows: could a new episode of tectonic activity exert forces on rock bridges , found at a candidate site, of such magnitudes that some of those bridges fail?

Basically, the failure of a bridge in between two roughly aligned finite fractures could mean that, at least, one new fracture would propagate between the nearest tips of the two fractures in question. Should this occur, the two newly connected fractures may mechanically act as a larger single fracture and, as a result, larger shear displacement may occur.

Assume a fracture with an approximate trace length of 100 meters, neighboring a canister hole, was looked upon as safe from the view point of the mechanical integrity of a canister hole / canister. If the fracture were connected to a second fracture of roughly the same size by tectonic forces, would the newly-formed fracture endanger the safety of the canister / canister hole by a comparatively larger shear displacement that it would be expected to undergo?

2 CONDITIONS FOR PROPAGATION

The set of conditions that allows propagation of a fracture tip into the rock is not always met within a natural rock mass. In a typical situation, the shear displacement of a fracture is accompanied by the deformation of the two opposite fracture surfaces and the resultant displacement-deformation is accommodated within the fixed boundaries of the fracture. No enlargement beyond the fracture outline takes place. The set of conditions, however, may happen to allow propagation. This certainly calls for a closer look at the propagated part. Propagation of larger geological structures has usually been studied under predominantly in plane Mode II of loading , see Segall & Pollard (1980), Petit & Barquins (1988) and Li (1991).

In a previous study that included the use of the three dimensional Distinct Element code 3DEC, Itasca (2003), the conditions that would allow the propagation of a large, circular fracture periphery into the surrounding rock was studied, see Hakami (2006). The virtual rock and the large fracture contained in the numerical model were, pre-conditioned such that the extension of the fracture would be possible.

The pre-conditioning of the surrounding rock was made based on the following premises

- The propagation of the circular fracture was bound to take place in the plane of the fracture.
- The formation of a Propagation Bed, much larger than the fracture limits, preceded the emergence of the circular fracture.
- The strength of the Propagation Bed, which, compared with the rock mass, is reduced by a larger number of cracks and micro cracks, may be described by its "inherent" cohesion. In contrast to the " apparent"

cohesion, the inherent cohesion is the true cohesion that a rock, here the rock contained in the Propagation Bed, is able to secure, before a fully localized shear fracture emerges out of that rock.

- Upon the encroachment of the driving force, prevailing at the tip of the circular fracture, onto the surrounding rock, the inherent cohesion of the Propagation Bed is lost. The loss of inherent cohesion is immediately followed by frictional forces being mobilized, and the newly-extended portion of the circular fracture behaves thereupon following the Mohr-Coulomb criterion.

Figure 1 is an illustration of the progress in the formation of a fracture and its subsequent extension. Simplifications were made to include the process in the numerical model.

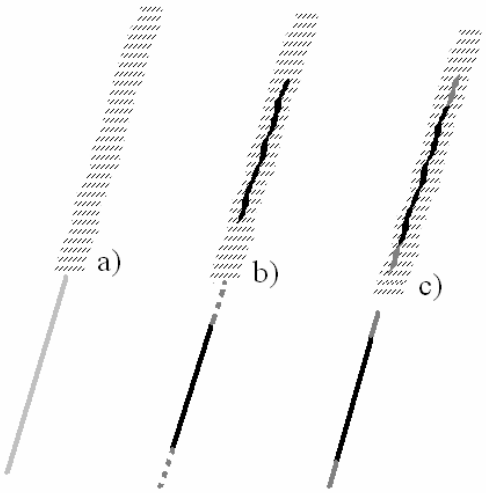

Figure 1. An illustration of the conditions for the localisation of a fracture and its subsequent propagation: a) Propagation Bed, b) Creation of the fracture and c) Propagation of the fracture. Simplified sketches at the lower half of the figure show how the process was incorporated into the numerical model

Inherent cohesion, which indeed is the adhesion between the grains of, e.g. a rock, is difficult to measure. Yet standard tests such as uniaxial compressive strength and uniaxial tensile strength (may also be obtained indirectly by Brazilian test) yield values that may be considered as measures of the inherent cohesion of a rock.

Figure 2 shows the range of values for the inherent cohesion, a selection of which may be made in order to enter the numerical computations.

3 THIS STUDY

In this study, a simple geometry was incorporated into a 3DEC , Itasca (2003) numerical simulation. The geometry chosen included two circular fractures, both belonging to the same oblique plane with a dip of 40 degrees and striking at right angle to the direction of the major principal stress σ_1. As shown in Figure 3, the distance between the two nearest tips of the two fractures, here may be called the Bridge Width, enters the computations as an input parameter.

Assume that the two circular fractures have a diameter of 100 meters each. After some introductory analyses, a Bridge Width of 60 meters was chosen to lie between the two fractures in the numerical model.

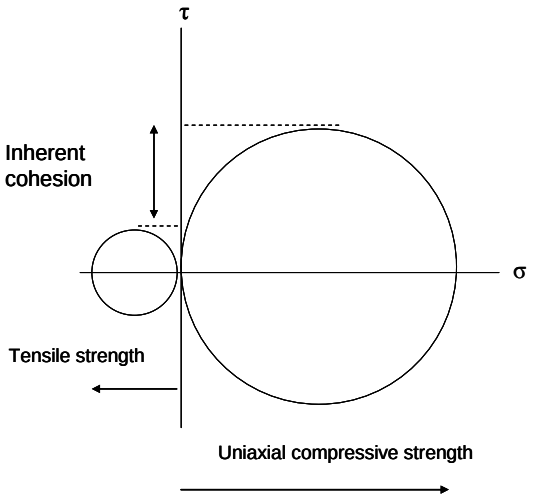

Figure 2. A tentative definition of the inherent cohesion. From the range shown, selected values entered the numerical computations.

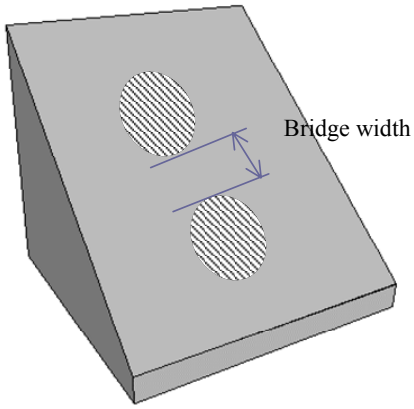

Figure 3. Sketch showing two circular fractures , bridge in between and the definition of the bridge width.

The input parameters selected were as follows:

a) *Rock Mass*
   $E_{Rock\ mass}$ = 40 GPa
b) *Fracture properties and size*
   Fracture Diameter = 100 m
   Kn = 1 GPa / m
   Ks = 0.3 GPa / m
   $\phi = 20°$
c) *Bridge*
   Kn = 10 GPa / m
   Ks = 3 GPa / m
   $\phi = 25°$

The expressions defining the in-situ stress field, valid for a depth range of 350-650 m, were borrowed from SKB, 2005:

$$\sigma_H = 35 + 0.020\ Z$$
$$\sigma_h = 19 + 0.025\ Z$$
$$\sigma_v = 0.0265\ Z$$

A hydrostatic pore pressure was included in the numerical model. The centre of the model block had a depth of 500 m; a depth relevant for the placement of a repository in Sweden.

Figure 4 shows the contours of the shear displacements across the plane containing the extended fractures. It is clear from the displacement contours that the two fractures are being sheared independently; larger shear displacements of around 20 mm occur at and around the centre of each fracture. The bridge, even though suffering from some damage (see later), does not fail mechanically.

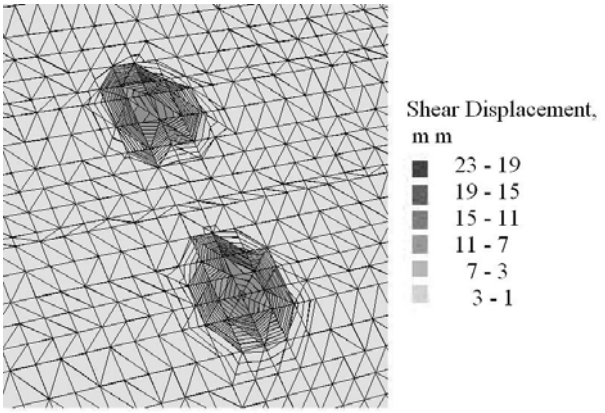

Figure 4. The shear displacement contours across the plane including the two fractures with a diameter of 100 m each. Maximum shear displacement of around 20 mm occurred at the central area of the fractures.

In the next analysis performed the Bridge Width was reduced to 30 meters. The results showed that the bridge failed in the sense that the two fractures involved became interconnected through a newly formed fracture and proceeded to behave as a single fracture. Figure 5 shows how the interconnection went on. To some extent, the two fractures behaved independently, but further shearing forced the two fractures to join and behave as if only one fracture existed.

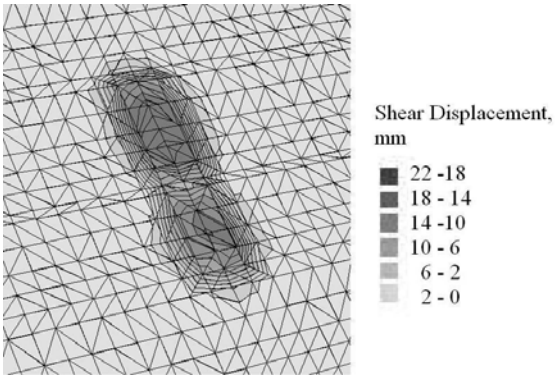

a)

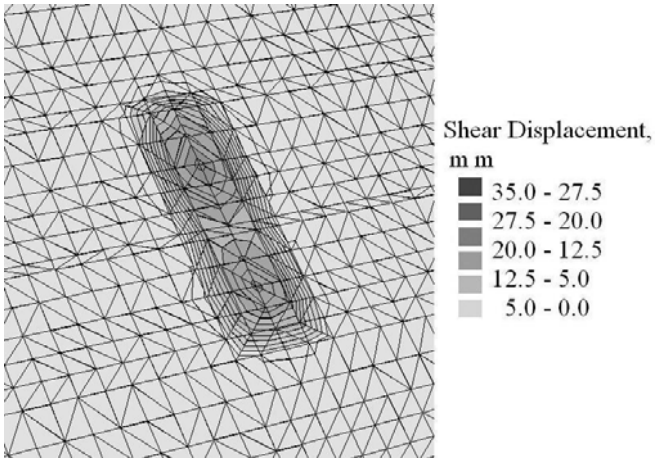

b)

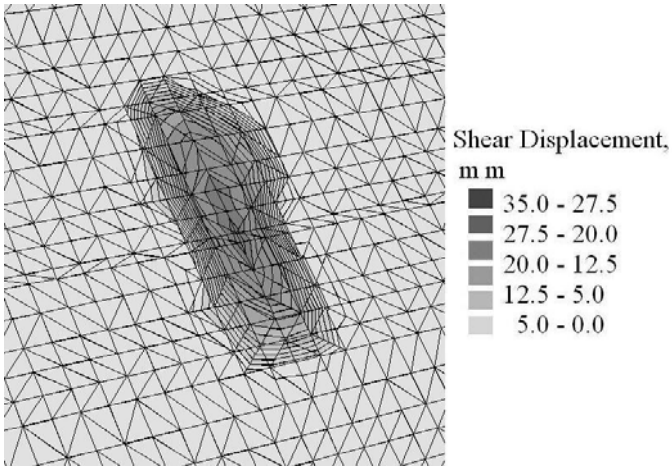

c)

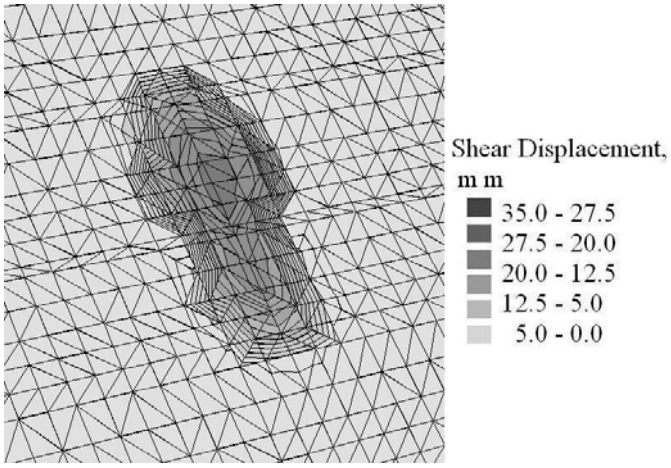

…d)

Fig 5, a) ,b), c) and d). Sequential stages in failure of a bridge. The bridge had a width of 30 meters.

4 DISCUSSION

It is informative to make comparisons between the maximum shear displacement a single, propagating fracture undergoes and the case where the same fracture is a member of the system fracture-bridge-fracture. Choosing one circular fracture with a diameter of 100 m - which was set to propagate under an identical set of parameters as for the case of two fractures separated by a bridge with a width of 60 m – it was noted that the maximum shear displacement was nearly 25 mm. This is to compare with a maximum shear displacement of nearly 19 mm, where the fracture was a member of the system fracture-bridge-fracture (Figure 4). It should be evident that the discrepancy has to do with the fact that the same reserve of energy – stored in two identical model blocks, containing one and two fractures - was expended on propagating / displacing one and two fractures respectively.

Despite the fact that the analysis incorporating a bridge with a width of 60 meters shows that the bridge does not fail; i.e. the two fractures involved remain to behave independently, it is informative to look for how far from the initial outlines the propagations associated with the two fractures may have reached.

Figure 6 shows the shear displacement contours taken from the same analysis but plotted in the narrow range of 0.0 – 0.85 mm. It is interesting to note that the propagation has indeed proceeded in form of patches sheared not more than – on average - about 0.15 mm and that the two fractures have been interconnected by two of those patches. This connectivity, which was noticed had no effect on the mechanical integrity of the bridge, could result in hydraulic connectivity. One would perhaps become concern about the role such hydraulic inter-connectivity may play as regards the safety of a canister hole / canister.

Trying to translate the above finding - which so far is just a product of the numerical investigation reported - to the sphere of natural rock fractures, one may speculate that a natural fracture that evidently has extended beyond its outermost boundary may even have propagated to a much larger area, without the propagation being detected by the naked eye. One should then make a distinction between visible and invisible parts of a propagated fracture in order to draw conclusions out of a wider perspective.

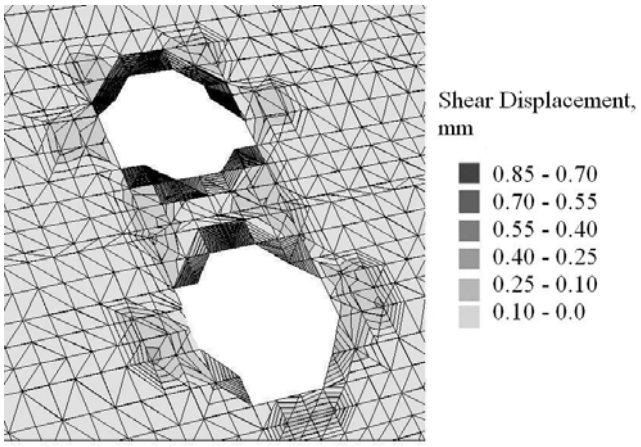

Figure 6. Shear displacement contours of the same two fractures as shown on Figure 4. Because of the very small range of shear displacements deliberately chosen (less than one mm), the contours of the much larger displacements occurring at the central parts of the fractures (larger than few mm) are plotted erroneously and were removed from the figure.

ACKNOWLEDGEMENT

This work was financed by the Swedish Nuclear Waste Management Co (SKB), contract 10008.

REFERENCES

Hakami, H. 2006. 4th Asian Rock Mechanics Symposium, ed. C. F. Leung & Y. X. Zhou, Singapore. Published by Word Scientific.

Itasca. 2003. 3DEC manuals, Itasca Consulting Group Inc. Minneapolis, USA.

Li, V C. 1991. "Mechanics of shear rupture applied to earthquake zones". In Atkinson, K B (ed). "Fracture mechanics of rock". Academic Press, London. : 351-428.

Petit, J-P, Barquins, M. 1988. Can natural faults propagate under mode ii conditions? Tectonics, 7(6), 1243-1256.

Segall, P & Pollard, DD. 1980. Mechanics of discontinuous faults. *J. geophys*. Res 85, 4337-4350

Shen, B. 1993. Mechanics of fractures and intervening bridges in hard rock. Doctoral thesis, Royal Institute of Technology, Stockholm, Sweden.

SKB. 2005. preliminary site description, Forsmark area – version 1.2. Swedish Nuclear Fuel and Waste Management Co, Report R-05-18, Stockholm, Sweden.

The Mogi-Coulomb True-Triaxial Failure Criterion and some Implications for Rock Engineering

Adel M. Al-Ajmi
Department of Petroleum Engineering, Sultan Qaboos University, Muscat, Oman

Robert W. Zimmerman
Division of Engineering Geology, KTH, Stockholm, Sweden

ABSTRACT: Most analyses of rock mechanics problems that involve failure or potential failure utilize Mohr's assumption that failure is controlled only by the minimum and maximum principal stresses, σ_1 and σ_3. However, evidence has been accumulating for several decades that the intermediate stress has a "strengthening effect", in the sense that, for a given value of σ_3, the value of σ_1 required to cause failure will be higher if $\sigma_2>\sigma_3$ than it would be if $\sigma_2=\sigma_3$. Mogi proposed that the failure criterion should be of the form $\tau_{oct} = f(\sigma_{m,2})$, where τ_{oct} is the octahedral shear stress, and $\sigma_{m,2} = (\sigma_1+\sigma_3)/2$. Analysis of many sets of data from the literature shows that most can be fit reasonably well with a linearized form of Mogi's criterion, $\tau_{oct} = a+b\sigma_{m,2}$. This criterion has several advantages: it accounts for the strengthening effect of σ_2, the coefficients a and b can be expressed in terms of the cohesion and coefficient of internal friction that appear in the Mohr-Coulomb criterion, and its linear form allows it to be used in analyzing engineering problems. For the specific problem of the stability of a vertical borehole, this criterion leads to substantially different predictions for the minimum required mud weight, as compared to those found using the Mohr-Coulomb criterion.

1 INTRODUCTION

Among the large number of shear failure criteria that have been proposed for rocks, the Mohr-Coulomb criterion is the most commonly used in practice. There are two major components of this criterion. The first is the assumption that, at failure, the major principal stress σ_1 is a linearly increasing function of the minor principal stress, σ_3. The second aspect is the assumption that the value of the intermediate principal stress, σ_2, has no influence on the rock strength.

Neither of these assumptions is precisely true for most rocks. Failure data for most rocks shows a nonlinear failure envelope with a negative second derivative, although the degree of nonlinearity varies from rock to rock. Much effort has been expended over recent years on deriving nonlinear failure criteria. These are typically fit to traditional failure data in which $\sigma_2=\sigma_3$, and are then used under the implicit assumption that, if $\sigma_2>\sigma_3$, failure will not depend on the actual numerical of σ_2

However, evidence has been accumulating over the past several decades to suggest that the intermediate principal stress does have an influence on rock strength (Handin 1967, Hoskins 1969, Mogi 1971, Haimson 2002). Many sets of such data have recently been collected by Colmenares & Zoback (2002), and in the monograph by Mogi (2006). A striking example of the extent to which real rock failure data may not comply with the assumption that failure depends only on σ_1 and σ_3 is shown in Figure 1, replotted from Haimson & Song (1995). The data from borehole breakouts, which occur under a true-triaxial stress state, clearly do not fall near the curve obtained from traditional ($\sigma_2=\sigma_3$) triaxial compression tests.

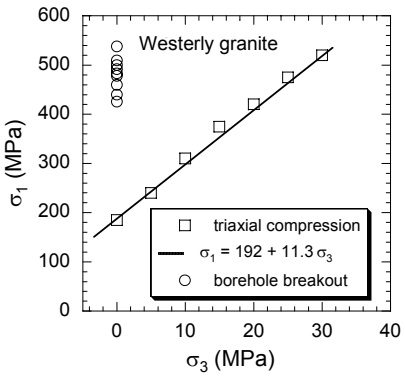

Figure 1. Failure data from Haimson & Song (1995) on Westerly granite, obtained under traditional triaxial compression ($\sigma_2=\sigma_3$) and true-triaxial ($\sigma_2>\sigma_3$) stress conditions.

Nevertheless, the use of true-triaxial failure criteria for analysis or design purposes has progressed very slowly. Three reasons may be hypothesised for this: (a) a reluctance to accept that the influence of σ_2 is a real attribute of rock rather than an experimental artifact, (b) the lack of well-validated true-triaxial failure criteria, and (c) the additional mathematical complexity that results when analyzing problems using a true-triaxial failure criterion. In this paper, and more so in some other recent papers that we summarize below, each of these three issues is addressed. First, by examining data from the literature, it is found that the influence of σ_2 on failure is the rule, rather than the exception. Next, a simple but relatively accurate true-triaxial failure law whose parameters can be obtained from traditional $\sigma_2=\sigma_3$ data is proposed and validated. Finally, it is shown that it is indeed practical to use this new true-triaxial criterion in rock mechanics analysis, specifically using it to examine the stability of vertical boreholes.

2 REVIEW OF VARIOUS FAILURE CRITERIA

Coulomb suggested that failure in compression takes place when the shear stress, τ, on any plane reaches a value that is sufficient to overcome both the natural cohesion of the rock plus the frictional force that opposes motion along that plane. The criterion can be written as

$$\tau = c + \sigma_n \tan\phi, \tag{1}$$

where σ_n is the normal stress on the failure plane, c is the cohesion, and ϕ is the angle of internal friction. Since criteria (1) will always first be satisfied on a plane that lies in the direction of σ_2, the value of σ_2 will not influence σ_n or τ, and so this failure criterion implicitly assumes that σ_2 has no effect on failure. The Coulomb criterion can also be expressed in terms of the maximum shear stress, τ_{max}, and the "effective mean stress", $\sigma_{m,2}$ (Jaeger et al. 2007):

$$\tau_{max} = c\cos\phi + \sin\phi\,\sigma_{m,2}, \tag{2}$$

$$\text{where} \quad \tau_{max} = (\sigma_1 - \sigma_3)/2, \quad \sigma_{m,2} = (\sigma_1 + \sigma_3)/2. \tag{3}$$

From this form of the Coulomb criterion, it is seen that the stress that resists the creation of a failure plane is $\sigma_{m,2}$.

Mohr generalized the Coulomb criterion by suggesting that, at failure, the normal and shear stresses across the failure plane are related by

$$\tau = f(\sigma_n). \tag{4}$$

A linear form for the function f is equivalent to the Coulomb criterion. Consequently, the failure criterion (1) is often known as the "Mohr-Coulomb" criterion.

Incorporation of the effect of σ_2 into failure criteria occurred earlier in soil mechanics than in rock mechanics. Drucker & Prager (1952) proposed a criterion of the form

$$\tau_{oct} = k + m\sigma_{oct}, \tag{5}$$

where τ_{oct} and σ_{oct} are the octahedral shear stress and octahedral normal stress, respectively, defined by

$$\tau_{oct} = (1/3)[(\sigma_1-\sigma_2)^2 + (\sigma_2-\sigma_3)^2 + (\sigma_3-\sigma_1)^2]^{1/2}, \tag{6}$$

$$\sigma_{oct} = (\sigma_1 + \sigma_2 + \sigma_3)/3, \tag{7}$$

where k and m are material constants. Although there seems to be little experimental evidence that this criterion is applicable to rocks, it continues to be occasionally used in petroleum geomechanics analysis.

Mogi (1971) verified experimentally that brittle fracture always occurs along a plane striking in the σ_2 direction. He also found that the intermediate principal stress indeed has a strengthening effect. Mogi concluded that the mean normal stress that opposes the creation of the fracture plane is $\sigma_{m,2}$, rather than the octahedral normal stress, σ_{oct}, since the fracture plane strikes in the σ_2 direction. Subsequently, Mogi suggested a new failure criterion of the form

$$\tau_{oct} = f(\sigma_{m,2}). \tag{8}$$

The function f is usually taken to be a power-law. Such a criterion has been criticized because its parameters cannot be easily related to the Coulomb parameters, c and ϕ (Colmenares & Zoback 2002). To circumvent this problem, and to simplify borehole stability analysis, Al-Ajmi & Zimmerman (2005) proposed taking f to be a linear function,

$$\tau_{oct} = a + b\sigma_{m,2}. \tag{9}$$

For conventional triaxial tests, $\sigma_2=\sigma_3$, and we have

$$\tau_{oct} = \sqrt{2}(\sigma_1-\sigma_3)/3. \tag{10}$$

The linear Mogi criterion, Equation (9), then reduces to

$$\sqrt{2}(\sigma_1-\sigma_3)/3 = a + b(\sigma_1+\sigma_3)/2. \tag{11}$$

Comparison with Equations (2,3) shows that for traditional triaxial data, the linear Mogi criterion coincides with the Coulomb criterion, if we make the following identification:

$$a = (2c\sqrt{2}/3)\cos\phi, \quad b = (2\sqrt{2}/3)\sin\phi. \tag{12}$$

Hence, for triaxial stress states ($\sigma_2=\sigma_3$) the linear Mogi criterion given by Equation (9) is exactly equivalent to the Coulomb criterion.

Al-Ajmi & Zimmerman (2005) searched the literature for polyaxial failure data, and located eight data sets: Dunham dolomite, Solenhofen limestone, Mizuho trachyte, coarse-grained dense marble, Shirahama sandstone, Yuubari shale, KTB amphibolite, and Westerly granite. The original sources of these data can be found in Al-Ajmi & Zimmerman (2005) and Colmenares & Zoback (2002). In each case, the data fall more nearly on a single curve if plotted in the Mogi plane, (τ_{oct},$\sigma_{m,2}$), than if plotted in either the Mohr plane, (τ_{max},$\sigma_{m,2}$), or the Drucker-Prager plane, (τ_{oct},σ_{oct}). Figure 2 shows the KTB amphibolite tested by Chang & Haimson (2000). The traditional triaxial data are shown as large black circles, along with the best-fitting straight line; the true-triaxial data are plotted as empty circles. The data fall most nearly on a single curve when plotted using Mogi's variables. This conclusion is not tied to the use of a linear failure criterion: when using the Drucker-Prager variables, the data show much scatter, and no curve, linear or not, can give a good fit.

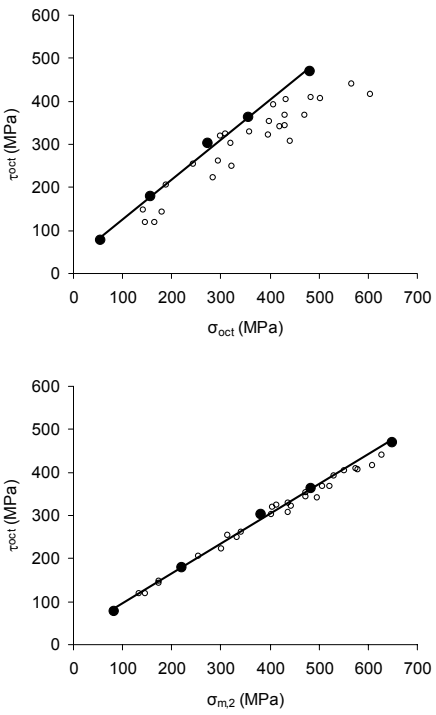

Figure 2. Failure criteria based on traditional triaxial test data (black circles), compared with true-triaxial test data (empty circles) for KTB amphibolite: (top) Drucker-Prager, (bottom) Mogi-Coulomb.

3 STRESSES AROUND A VERTICAL BOREHOLE

Drilling a borehole will alter the in situ principal stresses, which usually are the vertical stress (σ_v) and the maximum and minimum horizontal stresses (σ_H and σ_h). This leads to a stress concentration around the borehole. In a linear elastic material, the largest stress concentration occurs at the borehole wall. Therefore, borehole failure is expected to initiate there.

According to the Kirsch solution, the stresses at a vertical borehole wall are given by (Jaeger et al. 2007)

$$\sigma_r = P_w, \tag{13}$$

$$\sigma_\theta = \sigma_H + \sigma_h - 2(\sigma_H - \sigma_h)\cos 2\theta - P_w, \tag{14}$$

$$\sigma_z = \sigma_v - 2\nu(\sigma_H - \sigma_h)\cos 2\theta, \tag{15}$$

where σ_r is the radial stress, σ_θ is the tangential stress, σ_z is the axial stress, P_w is the internal borehole pressure, and ν is the Poisson ratio of the rock. The angle θ is measured clockwise from the σ_H direction. Since there are no shear stresses, σ_r, σ_θ and σ_z are the principal stresses.

Inspection of Equations (14,15) reveals that the tangential and axial stresses reach a maximum at $\theta = \pm\pi/2$, and a minimum at $\theta = 0$ or π. These critical positions remain the same for any values of the in situ stresses. Hence, we know a priori that failure can occur only at these points.

The tangential and radial stresses in Equations (13,14), σ_θ and σ_r, are functions of the mud pressure, P_w, but the vertical stress σ_z is not. Hence, any changes in the mud pressure will only affect σ_θ and σ_r. There consequently are two possible cases: either $\sigma_\theta \geq \sigma_r$, or $\sigma_r \geq \sigma_\theta$, which are associated with borehole collapse or hydraulic fracturing, respectively. The case of fracturing is discussed by Al-Ajmi & Zimmerman (2006a), and due to space limitations will not be repeated here, where we focus on borehole collapse. When P_w decreases, σ_θ increases towards the compressive strength of the rock. Thus, the lower limit of the mud pressure, P_{wb}, is associated with borehole collapse, in which σ_θ should be greater than σ_r. Bearing in mind this constraint, there are three permutations of the three principal stresses that need to be investigated in order to determine the minimum allowable mud pressure: (1) $\sigma_z \geq \sigma_\theta \geq \sigma_r$, (2) $\sigma_\theta \geq \sigma_z \geq \sigma_r$, and (3) $\sigma_\theta \geq \sigma_r \geq \sigma_z$. The compressive strength of the rock will first be exceeded at the position associated with the maximum value of σ_θ or σ_z (i.e., $\theta = \pm\pi/2$), and so the principal stresses at the borehole wall become

$$\sigma_r = P_w, \quad \sigma_\theta = A - P_w, \quad \sigma_z = B, \tag{16}$$

$$\text{where} \quad A = 3\sigma_H - \sigma_h, \quad B = \sigma_v + 2\nu(\sigma_H - \sigma_h). \tag{17}$$

4 MOHR-COULOMB BOREHOLE ANALYSIS

Using the effective stress concept to account for the pore pressure, P_0, the Mohr-Coulomb criterion becomes

$$(\sigma_1 - P_0) = C_0 + q(\sigma_3 - P_0)\,. \tag{18}$$

Equation (18) can be rearranged into the form

$$\sigma_1 = C + q\sigma_3, \quad \text{where} \quad C = C_0 - P_0(q-1). \tag{19}$$

Consider now the case where $\sigma_z \geq \sigma_\theta \geq \sigma_r$. Applying the Mohr-Coulomb failure criterion as expressed by Equation (2), and introducing Equation (19), the lower limit of the mud pressure corresponding to case 1, P_{wb1}, is given by

$$P_{wb1} = (B - C)/q. \tag{20}$$

Following the same procedure, the minimum allowable mud pressures corresponding to the other two cases are shown in Table 1.

Table 1. Collapse pressure in vertical boreholes (Mohr-Coulomb).

Case	$\sigma_1 \geq \sigma_2 \geq \sigma_3$	Minimum required P_{wb}
1	$\sigma_z \geq \sigma_\theta \geq \sigma_r$	$P_{wb1} = (B-C)/q$
2	$\sigma_\theta \geq \sigma_z \geq \sigma_r$	$P_{wb2} = (A-C)/(1+q)$
3	$\sigma_\theta \geq \sigma_r \geq \sigma_z$	$P_{wb2} = A - C - qB$

As the mud pressure decreases, the principal stresses will alternate from one case to another. Therefore, the collapse pressures given in Table 1, should be used to recalculate the principal stresses (σ_r, σ_θ, σ_z) by applying Equations (13-15), where $P_w = P_{wb}$. For each case, the principal stresses are then substituted into Equation (20). The lower limit of mud pressure is associated with the case in which the principal stresses have satisfied the Mohr-Coulomb criterion.

In the field, generally, borehole collapse corresponds to case 1 or case 2, where the radial stress is the minimum principal stress. It would be advantageous if the mud pressure related to these two common cases could be determined from one single equation. After some mathematical manipulation, the lower limit of the mud pressure corresponding to these cases becomes

$$P_{wb} = (S + \sqrt{R})/2(q + q^2), \tag{21}$$

where S and R are given by

$$S = Aq - C(1+2q) + B(1+q), \tag{22}$$

$$R = B^2(1+2q+q^2) - 2AB(q+q^2) - 2BC(1+q) + (Aq+C)^2. \tag{23}$$

5 MOGI-COULOMB BOREHOLE ANALYSIS

In terms of the first and second stress invariants, I_1 and I_2, defined by

$$I_1 = \sigma_1 + \sigma_2 + \sigma_3, \quad I_2 = \sigma_1\sigma_2 + \sigma_2\sigma_3 + \sigma_3\sigma \tag{24}$$

and utilizing the effective stress concept, the Mogi-Coulomb criterion can be expressed as

$$(I_1^2 - 3I_2)^{1/2} = a' + b'(I_1 - \sigma_2 - 2P_0) \tag{25}$$

$$\text{where} \quad a' = 2c\cos\phi\,, \quad b' = \sin\phi \tag{26}$$

There are six permutations of the principal stresses ($\sigma_r, \sigma_\theta, \sigma_z$) that needed to be investigated. Since the first and second stress invariants have the same form in all the cases, only the intermediate principal stress will vary from one case to another, as per Equation (25). Consequently, the six permutations of the principal stresses can be represented by three scenarios in which σ_2 can be σ_θ, σ_z, or σ_r.

The principal stresses at the borehole wall given by Equation (16) represent the highest stress concentration that may result in compressive failure. By introducing Equation (16) into Equation (24), the stress invariants are given by

$$I_1 = A + B, \quad I_2 = AB + AP_w - P_w^2. \tag{27}$$

Consider the scenario of borehole collapse, where $\sigma_2=\sigma_\theta=A-P_w$ and $P_w=P_{wb1}$. Implementing the Mogi-Coulomb failure criterion as formulated by Equation (25), and introducing Equation (27), gives

$$[(A+B)^2-3(AB+AP_{wb1}-P_{wb1}^2)]^{1/2}-bP_{wb1}=K, \quad (28)$$

where $K = a' + b'(B - 2P_0)$ (29)

Solving this equation for P_{wb1} will give two roots. Since we are concerned with borehole collapse, the smaller root is the lower limit of the mud pressure, that is,

$$P_{wb1} = \{3A + 2b'K - [H + 12(K^2 + b'AK)]^{1/2}\}/(6 - 2b'^2). \quad (30)$$

$$H = A^2(4b'^2 - 3) + B(B - A)(4b'^2 - 12). \quad (31)$$

Similarly, the minimum allowable mud pressures corresponding to the other stress states are listed in Table 2, where $G = K+b'A$, and all other parameters are as defined previously.

However, borehole collapse will usually be related to case 1 and case 2. For case 1 to occur, it must be the case that

$$\sigma_z \geq \sigma_\theta. \quad (32)$$

Introducing Equations (16,17) into Equation (32) gives

$$\sigma_v \geq \sigma_H(3-2\nu) - (1-2\nu)\sigma_h - P_w. \quad (33)$$

Considering the practical range of Poisson's ratio (0–0.5), and the facts that the ratio of maximum horizontal stress to minimum horizontal stress (σ_H/σ_h) typically ranges from 1 to 2, and that the collapse pressure will not exceed the minimum in situ stress in Equation (33), it follows that the vertical stress must be greater than the maximum horizontal stress for case 1 to develop. Therefore, case 1 is only associated with the normal faulting stress regime (i.e., $\sigma_v \geq \sigma_H \geq \sigma_h$), whereas case 2 may develop in any stress regime. In the field, consequently, case 2 (i.e., $\sigma_\theta \geq \sigma_z \geq \sigma_r$) will be the most commonly encountered stress state corresponding to borehole collapse for all stress regimes.

Table 2. Collapse pressure in vertical boreholes (Mogi-Coulomb).

Case	Minimum required mud pressure, P_{wb}
$\sigma_z \geq \sigma_\theta \geq \sigma_r$	$\{3A+2b'K - [H+12(K^2+b'AK)]^{1/2}\}/(6-2b'^2)$
$\sigma_\theta \geq \sigma_z \geq \sigma_r$	$A/2-\{12[a'+b'(A-2P_0)]^2 - 3(A-2B)^2]\}^{1/2}/6$
$\sigma_\theta \geq \sigma_r \geq \sigma_z$	$\{3A-2b'G - [H+12(G^2-b'AG)]^{1/2}\}/(6-2b'^2)$

6 COLLAPSE PRESSURE EVALUATIONS IN TYPICAL FIELD CONDITIONS

Al-Ajmi & Zimmerman (2005, 2006a, 2006b) performed borehole stability analysis for vertical, deviated and horizontal boreholes, in various stress regimes. They also examined some oilfield data from the North Sea and Indonesia in light of the Mohr-Coulomb and Mogi-Coulomb criteria. Here we summarize one of these cases.

Consider a vertical borehole drilled in a sandstone formation from the Cyrus reservoir in the UK continental shelf, at a depth of about 2600 m (McLean & Addis 1990). The sandstone has a cohesion of 6 MPa and a friction angle of 43.8°. The vertical stress and the formation pore pressure gradients are taken to be σ_v=22.6 kPa/m and P_0=10.2 kPa/m. The in situ horizontal stresses were assumed to be isotropic, with a gradient of 17 kPa/m. At the depth of interest, using the Mohr-Coulomb borehole failure criterion, Table 1 gives $P_{wb}=P_{wb2}$=27,632 kPa. Hence, the minimum overbalance pressure ($P_{well} - P_{pore}$) is 1112 kPa. At the same depth, the Mogi-Coulomb borehole failure criterion gives $P_{wb} = P_{wb2}$ = 27,015 kPa, and the minimum overbalance pressure becomes 495 kPa. The two borehole failure criteria lead to quite different values for the collapse pressure.

7 CONCLUSIONS

The Mogi-Coulomb failure criterion, which incorporates the effect of the intermediate principle stress, is able to fit true-triaxial failure date for many rocks. When incorporated into borehole stability analysis, it leads to much less conservative predictions of the required mud pressure than would be obtained using the Mohr-Coulomb criterion. Other engineering implications of this true-triaxial failure criterion remain to be investigated.

REFERENCES

Al-Ajmi, A.M. & Zimmerman, R.W. 2005. Relation between the Mogi and Coulomb failure criteria. *International Journal of Rock Mechanics* 42:431-439.

Al-Ajmi, A.M. & Zimmerman, R.W. 2006a. Stability analysis of vertical boreholes using the Mogi-Coulomb failure criterion, *International Journal of Rock Mechanics* 43:1200-1211.

Al-Ajmi, A.M. & Zimmerman, R.W. 2006b. Stability analysis of deviated boreholes using the Mogi-Coulomb failure criterion, with applications to some oil and gas reservoirs. In *Proc. SPE Asia-Pacific Drilling Tech. Conf.,* Bangkok, 13-15 November 2006, paper SPE 104035.

Chang, C. & Haimson, B. 2000. True triaxial strength and deformability of the German Continental deep drilling program (KTB) deep hole amphibolite. *Journal of Geophysical Research* 105:18,999-19,013.

Colmenares, L.B. & Zoback, M.D. 2002. A statistical evaluation of intact rock failure criteria constrained by polyaxial test data for five different rocks. *International Journal of Rock Mechanics* 39:695-729.

Drucker, D.C. & Prager, W. 1952. Soil mechanics and plastic analysis or limit design. *Quarterly Journal of Applied Mathematics* 10:157-165.

Haimson, B.C. & Chang, C. 2002. True triaxial strength of the KTB amphibolite under borehole wall conditions and its use to estimate the maximum horizontal in situ stress. *Journal of Geophysical Research - Solid Earth* 107(B10): art. no. 2257.

Haimson, B.C. & Song, I.S. 1995. A new borehole failure criterion for estimating *in situ* stress from breakout span. In T. Fujii (ed.), *Proc. 8th Int. Cong. Rock Mech.*, vol. 1, Rotterdam: Balkema, pp. 341-346.

Handin J., Heard, H.C. & Magouirk, J.N. Effect of the intermediate principal stress on the failure of limestone, dolomite, and glass at different temperature and strain rate. *Journal of Geophysical Research* 72:611-640.

Hoskins, E.R. 1969. The failure of thick-walled hollow cylinders of isotropic rock. *International Journal of Rock Mechanics* 6:99-116.

Jaeger, J.C., Cook, N.G.W. & Zimmerman, R.W. 2007. *Fundamentals of Rock Mechanics,* 4th ed. Oxford: Blackwell.

McLean, M. & Addis, M. 1990. Wellbore stability: The effect of strength criteria on mud weight recommendations. In *Proc. 65th Ann. Tech. Conf. Exh. SPE*, New Orleans, 23-26 Sept. 1990, paper SPE 20405.

Mogi, K. Fracture and flow of rocks under high triaxial compression. *Journal of Geophysical Research* 1971;76(5):1255-1269.

Failure mechanisms around shallow tunnels in brittle rock

D. Saiang & E. Nordlund
Division of Mining and Geotechnical Engineering, Luleå University of Technology, Sweden

ABSTRACT: As part of an ongoing study on the mechanical characteristics of the damaged rock zone (DRZ) around a tunnel boundary and its influence on the overall behaviour of the near-field host rock, a numerical study was conducted to investigate the dominant rock mass failure mechanisms around shallow tunnels located in a body of brittle rock mass. Preliminary studies have clearly indicated that, the rock mass behaviour was largely dictated by the different yield mechanisms involved. These mechanisms appear to be multifarious due to the complex state of the induced stresses around the tunnel boundary at shallow depth. Some of these yield mechanisms are often difficult to capture using the traditional yield criterion such as the Mohr-Coulomb. In the study reported in this paper a series of computer simulations were performed using typical in-situ stresses and rock mass conditions generally encountered in shallow tunnelling projects in Sweden. The presence of a disturbed/damaged rock zone with finite thickness was also added into the models. Due to the nature of the simulations the FLAC2D code was selected and used. The values for the input parameters were estimated using a systematic procedure. To prevent premature tensile yielding due to transient loading traction was applied during tunnel excavation. The results show that, the dominant yield mechanism occurring around the shallow tunnel in brittle rock is the one of tensile nature. Compressive mechanisms do occur but seems to be less critical to overall performance of the tunnel. However, they do influence the overall behaviour of the rock mass response. The results further indicated that, the 'true' locality of instability could be predicted from elastic analyses, by observing if all the major principle stresses are in tension in that locality. The shear strain increment plots of the model in plastic mode further supported this observation.

1 INTRODUCTION

Rock mass failure can occur either as gravity driven fallouts or stress driven failures. The former is usually associated with shallow and surface excavations, while the latter with deep excavations. However, experience has shown that both can occur irrespective of depth, dependent on the state of stress and rock mass characteristics (Diederichs, 1999). With the Swedish rock mass conditions and the state of stresses both of these failure types are evident even at very shallow depths (0-20 m).

In this paper, as part of an ongoing study on the mechanical characteristics of the damaged rock zone (DRZ) around a tunnel boundary and its influence on the overall behaviour of the near-field host rock, the stress driven failures are investigated for shallow depth excavations. Typical in-situ stresses and rock mass conditions generally encountered in shallow tunnelling projects in Sweden are used. The rock mass is generally of good quality with brittle rock resemblance. Earlier studies of the same scenario by Saiang & Nordlund (2006) and Töyrä (2006) have clearly indicated that, the rock mass behaviour was largely dictated by the different yield mechanisms involved. These mechanisms appear to be multifarious due to the complex state of the induced stresses around the tunnel boundary. Some of these yield mechanisms are often difficult to capture using the traditional yield criterion such as the Mohr-Coulomb.

The results show that, the dominant yield mechanism occurring around the shallow tunnel in brittle rock is the one of tensile nature. Compressive mechanisms do occur but seem to be less critical to the overall performance of the tunnel. However, they do influence the overall behaviour of the rock mass response. The results further indicated that, the locality of instability could be predicted from simple elastic analysis. In particular by observing if all the major principle stresses are in tension in that locality. This observation was further supported by the shear or volumetric strain evaluations in the plastic analysis.

2 BACKGROUND

The mechanics of brittle failure near tunnel boundaries have been described in many rock mechanics texts (e.g. Hoek & Brown, 1980; Brady & Brown, 1985; Hoek et al, 1995) and articles (e.g. Stacey, 1981; Pelli et al, 1991; Martin et al, 1997; Read et al, 1998; Diederichs, 2003; Hajiabdolmajid et al, 2003). The various failure types and the mechanisms involved have also been described (e.g. Martin, 1997; Hajiabdolmajid et al, 2003; Diederichs, 2003).

The widely used yield criteria for rock mechanics analysis have been the Mohr-Coulomb (M-C) and Hoek-Brown (H-B). The normal assumption is that both criteria can simulate brittle and plastic behaviours. According to these yield criteria the assumptions for compressive and tensile failures can be summarized as follows:

For tensile failure to occur

$\sigma_3 \le \sigma_t$ and $\sigma_1 \le 0$ (1)

For compressive failure to occur

$\sigma_3 > \sigma_t$ and $\sigma_1 > \sigma_{1s}$ (2)

σ_{1s} is the peak strength of the rock mass along the failure curve at various stress states. The above assumptions are illustrated graphically in Figure 1 below in terms of the principle stresses:

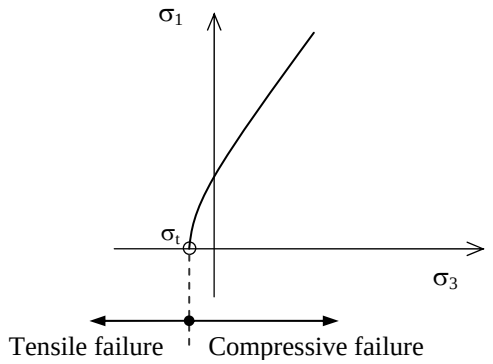

Figure 1. Failure assumptions according to H-B and M-C in terms of the principle stresses.

Although the tensile strength of the rock mass is accounted for in the two criteria the primary assumption however is that, failure is primarily due to compressive mechanisms, hence the compressive strength is important. The compressive strength according to the two criteria is provided by simultaneous mobilization of cohesion *(c)* and friction *(ϕ)*. However, it has been shown that under low confining stress conditions the yield process is governed by cohesion weakening and cohesion weakening – friction mobilisation phenomenon (e.g. Martin et al, 1997; Diederichs & Kaiser, 1999; Hajiabdolmajid et al, 2003). Under such circumstances the cohesion and tensile strength are considered important.

3 MODEL SETUP

3.1 *Model Geometry*

The model was based on one of the Swedish railroad administration's tunnel geometries. In this case a large single-track tunnel geometry was selected (see Figure 2). For the sake of numerical modelling the geometry has been slightly modified.

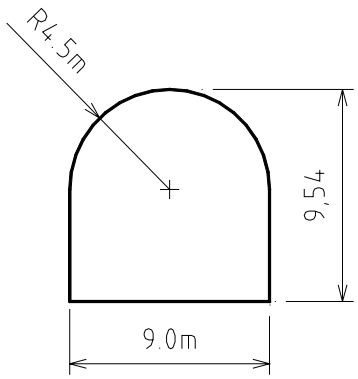

Figure 2. A large single-track railway tunnel geometry used in this study.

Figure 3 shows the model geometry in a FLAC2D model. A zone of finer grids is used near the excavation boundary while the outer zone comprises coarser grids. The sizes of the zones near the tunnel boundary are as small as 5 cm x 5 cm. The width and height of the model are large enough to account for large disturbances usually observed around near surface excavations.

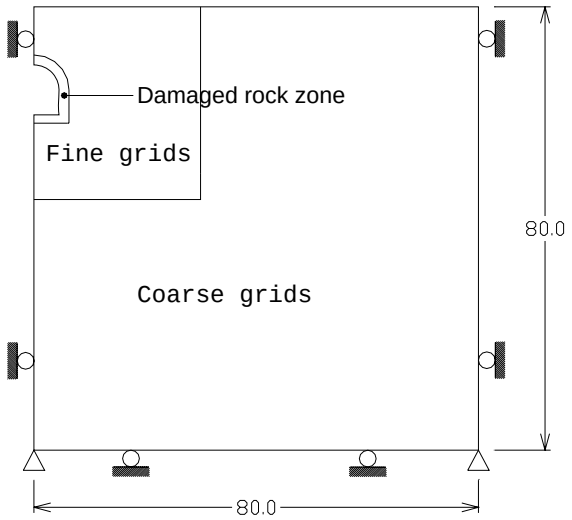

Figure 3. An 80 x 80 m symmetric model used in the numerical study. Finer grids are used near the tunnel boundary while coarser grids are used away from the tunnel boundary.

3.2 *Primary input parameters*

In this study we assume a rock mass that resembles the Swedish rock mass conditions. The Swedish rock mass is of an above average or good quality type, with brittle rock characteristics. The rock mass parameters are shown in Table 1. Using these parameters the elastic and plastic parameters of the rock mass were estimated.

Table 1. Rock parameters used in deriving the rock mass strength parameters.

Parameter	Value
Intact rock compressive strength, σ_{ci}	250 MPa
Geological strength index, *GSI*	60
Hoek-Brown rock constant, m_i	33

The in-situ stresses used in models are those reported by Stephansson (1993), which are based on hydraulic fracturing measurements. These are:

$$\sigma_V = \rho g z \quad (3a)$$
$$\sigma_H = 2.8 + 0.04z \quad (3b)$$
$$\sigma_h = 2.2 + 0.024z \quad (3c)$$

3.3 *Input parameters for the damaged rock*

The elastic parameters required are E_d (Young's modulus for damaged rock) and v_d (Poissons ratio for damaged rock). The Poissons ratio is assumed equal to a constant value of 0.25. Our assumption of the Young's Modulus for the damaged rock with respect to the undamaged rock is illustrated in Figure 4. For the damaged rock the magnitude of the Young's modulus is less than that of the undamaged rock. Because the depth of the damaged rock is small (<0.3 m) we assumed that any variation in the value of E_d would be very small and therefore negligible. For most drill and blast excavations the average modulus of the damaged rock around the tunnel boundary is about 70% of that of the undamaged rock (e.g. Priest, 2005). On this basis the base case E_d is estimated.

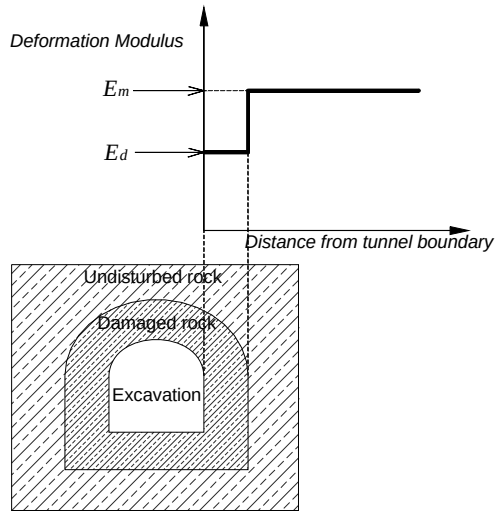

Figure 4. Assumption used for the Young's modulus (E) around the tunnel boundary. E_m and E_d are the Young's modulus for undamaged and damaged rock mass respectively.

3.4 *Strength parameters for the damaged rock*

By using the notion of disturbance factors, *D*, (Hoek et al, 2002) we estimated the strength parameters, *c* and ϕ, for the damaged rock mass using RocLab (Rocscience, 2005). We simply modified the value of *D* until the desired value of E_d is achieved then we determine the values for *c* and ϕ at that point. Note that, in our models we assume that the disturbance is in the form of damaged rock around the tunnel boundary.

A summary of the input parameters for the standard model is shown in Table 2. The input values were estimated using the 2002 version of the Hoek-Brown criterion (Hoek et al, 2002) and the systematic procedure described in Saiang and Nordlund (2007).

Table 2. Input parameters for the standard model.

Parameter	Value
For undamaged rock mass:	
Young's Modulus, *E*	17.8 GPa
Poisson's ratio, *v*	0.25
Cohesive strength, *c*	2.6 MPa
Friction angle, ϕ	67.8°
Tensile strength, σ_t	0.4 MPa
For damaged rock mass:	
Young's Modulus, E_d	12.5 GPa
Poisson's ratio, v_d	0.25
Cohesive strength, c_d	1.4 MPa
Friction angle, ϕ_d	64.3°
Tensile strength, σ_{td}	0.2 MPa

3.5 *Model scenarios*

Several scenarios (see Table 3) were simulated in order to study the response of the surrounding rock mass when various parameters are varied. Variations in the rock mass mechanical properties were only applied to the DRZ, while for the undamaged rock they remain unchanged at Case 0 values. Only one parameter was varied at a time while others were kept constant. Table 4 shows the variable parameter data set for the scenarios in Table 3. For case 7 the in-situ stresses were varied according to:

$$\sigma_V = \rho g z \ (\pm 20\%)$$
$$\sigma_H = 2.8 + 0.04z \ (\pm 50\%)$$
$$\sigma_h = 2.2 + 0.024z \ (\pm 50\%)$$

The standard model has a damaged rock zone, with a thickness of 0.3 m, around the tunnel boundary. The thickness conforms to the Swedish Railroad Administration criteria for tunnel damage control during excavation.

Table 3. Model scenarios.

Scenario	Description
Case 0:	Standard model
Case 1:	No damage zone
Case 2:	Varying Young's modulus of the DRZ
Case 3:	Varying compressive strength of the DRZ
Case 4:	Varying Tensile Strength of DRZ
Case 5:	Varying thickness of the DRZ
Case 6:	Varying overburden thickness
Case 7:	Varying in-situ stresses

Table 4. Variable parameter data set.

Scenario	Low	Standard	High
Case 0:	–	–	–
Case 1:	–	–	–
Case 2:	8.5GPa	11.8 GPa	17.8 GPa
Case 3:	8.8 MPa	12.7 MPa	26.8 MPa
Case 4:	0 MPa	0.2 MPa	1.2 MPa
Case 5:	0.1 m	0.3 m	1.0 m
Case 6:	2.0 m	10.0 m	20.0 m

4 RESULTS

4.1 *Failure modes and mechanisms*

4.1.1 *Elastic analysis*

An elastic analysis of the stresses around tunnel boundary revealed two types of failure modes and their potential localities. These are shown in Figure 5, which is based on the standard model. The damaged zone boundary has been omitted for the sake of clarity. Region A is where tensile failure will occur under 'biaxial extension' (i.e. $\sigma_3<\sigma_t$ and $\sigma_1<0$), while Region B is where tensile failure will occur from a compressive origin (i.e. $\sigma_3<\sigma_t$ and $\sigma_1>0$). Both failure types are of tensile nature but the mechanisms driving them are different. This will be further discussed in Section 5. Compressive failure ($\sigma_3>0$ and $\sigma_1>\sigma_{1s}$) is likely to occur in the roof and the toe of the tunnel.

Calculation of the strength factors are found to be less than 1.0 within regions A and B, but greater than 1.0 elsewhere.

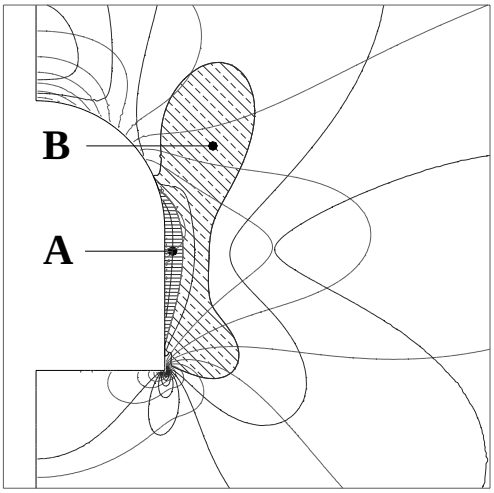

Figure 5. Regions of potential failures identified from elastic model. Region A is under biaxial extension ($\sigma_3<\sigma_t$ and $\sigma_1<0$), while region B is tensile failure under compressive mode ($\sigma_3<\sigma_t$ and $\sigma_1>0$).

4.1.2 *Plastic analysis*

In the plastic analyses only a plasticity plot is required to reveal the presence of failed zones. Figure 6 shows the plasticity plot for the standard model. Yielding covers a larger area than expected, which does not conform to the elastic observations shown in Figure 5. Furthermore, it is not consistent withpractical observations. A plot of the volumetric strain is then made, which is shown in Figure 7. Interestingly, the region in which volumetric strain (or dilation) occurred matched the region where failure through biaxial extension (i.e. Region B) was predicted. The depth of this dilated zone is about 0.20 m. This observation seems more realistic in practice as well.

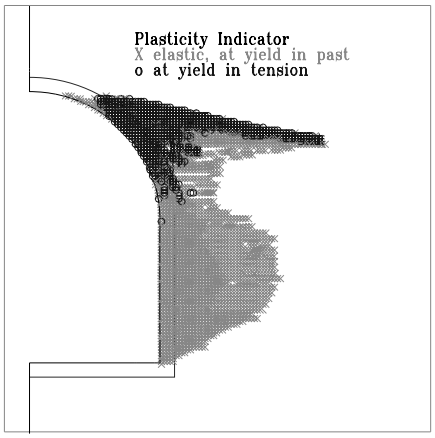

Figure 6. Plastic yielding resulting from input values for the strength parameters obtained by using the Hoek-Brown-GSI system. These values are shown in Table 2.

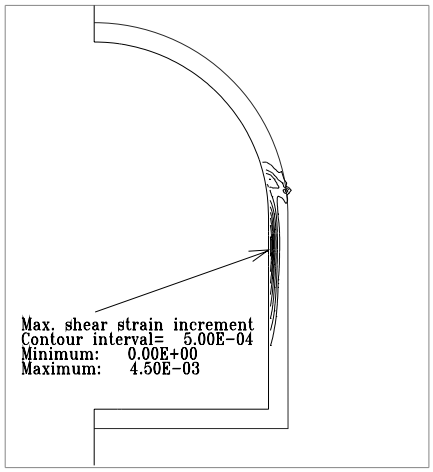

Figure 7. Shear/volumetric strains resulting from input values for the strength parameters shown in Table 2.

4.2 *Parameter Analysis*

Parameter analyses were conducted in line with the overall objective of the ongoing study on the mechanical behaviour of the damaged rock around a tunnel boundary. By varying the mechanical properties of the damaged rock mass and other parameters (see Tables 3) we investigated their effects in terms of variations in the magnitudes of the induced stress and displacement vectors.

4.2.1 *Effects on tangential stresses*

Figure 8 shows the effects on the tangential stresses for the various scenarios simulated. The percentage variations are calculated as maximum variations from the standard case scenario or Case 0. Observations were made at two locations around the tunnel boundary denoted A and B (see Figure 8). Point A is located on the tunnel boundary while Point B is located on the boundary between the damaged and undamaged rock. Observations at these two points were necessary in order to analyse the effect of the damaged rock with variations in its mechanical properties.

The tangential stresses are affected most by variations in the in-situ stresses compared to the other parameters tested. In terms of the inherent mechanical properties of the rock

mass, the Young's modulus when varied has notable effect on the tangential stresses. The thickness of the DRZ is significant in pushing high tangential stresses away from the tunnel boundary.

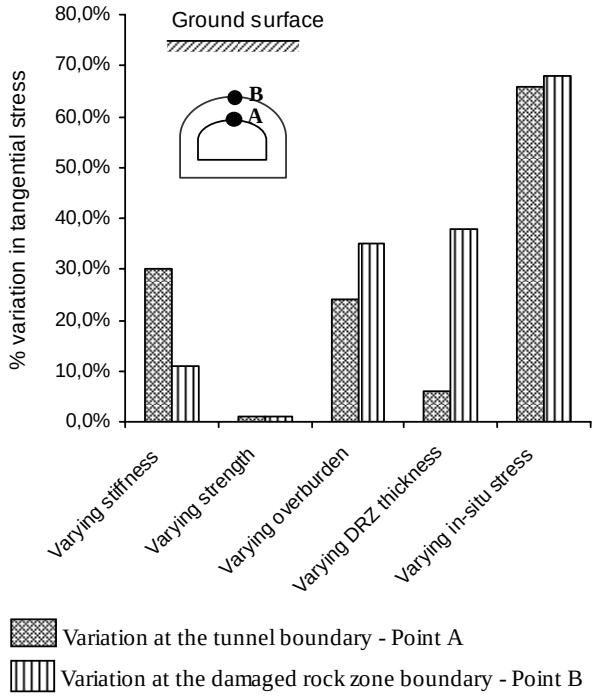

Figure 8. Percentage variation in the tangential stresses at two points (A and B) in the tunnel roof for the scenarios simulated.

The stress analyses also revealed a phenomenon that was dependent on the overburden. This is shown in Figure 9. The overburden was increased up to 500 m in order get a clear picture of this phenomenon. At depths less than 10 m the stresses are quite high since the body of rock above the tunnel behaves like a 'cantilever beam´. At depths greater than 10 m, it behaves like a normal rock mass. Coincidently, the 10 m overburden in the standard model appears to be the transition point.

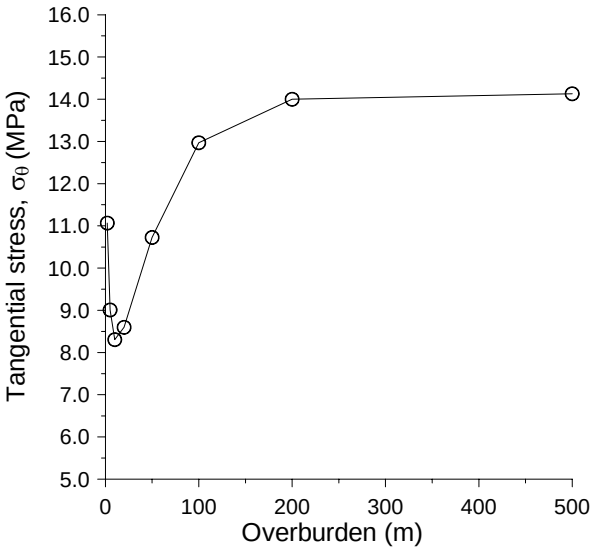

Figure 9. Effect of varying overburden on the tangential stress in the tunnel roof.

4.2.2 *Effects on ground deformation*

The ground deformation pattern observed is shown in Figure 10. Large deformations occur in the tunnel wall in the form of room closure, while roof diverges by smaller magnitudes. At the surface the ground heaves directly above the tunnel but subsides some distance away from the tunnel roof.

Figure 11 shows the maximum percentage variations in the wall deformation calculated against the base case deformations. The magnitude of the deformation is in the order of millimetres, with the highest value being 14 mm when the in-situ stresses were the maximum.

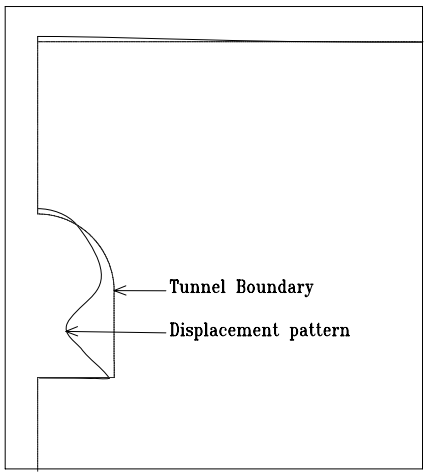

Figure 10. Ground deformation pattern observed. The walls converge and the roof diverges. At the surface the ground heaves directly above the tunnel and subsides approximately 15 m from the tunnel mid-centre.

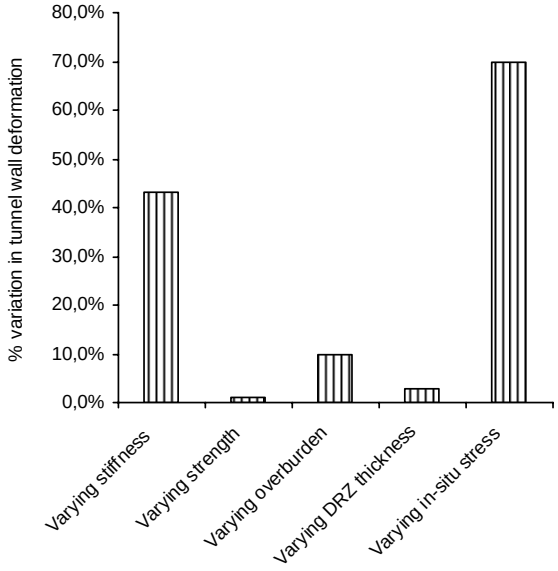

Figure 11. Percentage variation in the tunnel wall deformation for the different scenarios simulated.

5 DISCUSSIONS

5.1 *Failure mechanisms*

Two important failure mechanisms have been identified for the shallow tunnels investigated, codenamed Mode (I) and Mode (II). A third mechanism, codenamed Mode (III), is a minor one. The mechanisms are illustrated in Figure 12. Modes (I) and (II) affect the walls and the abutments, while Mode (III) affects the toe. The roof is affected by a combination of Modes (II) and (III). Of the three, Mode (I) is the most critical as the results have shown.

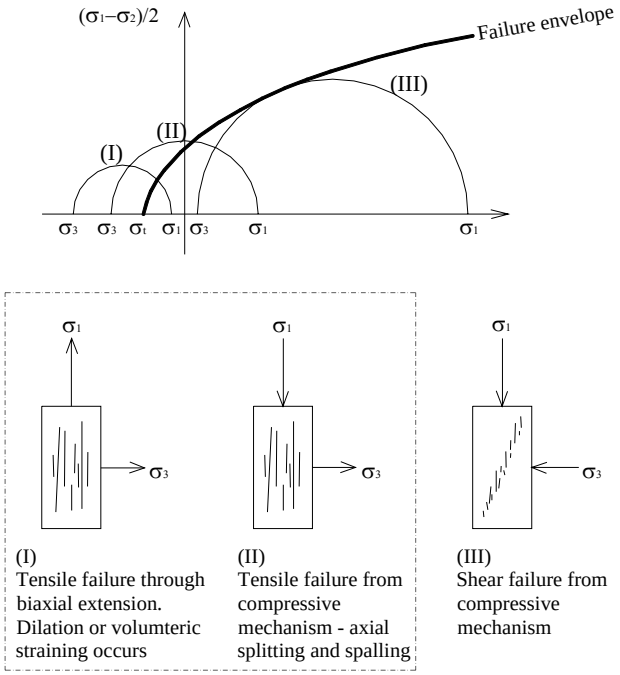

Figure 12. Potential failure types identified for the shallow excavations. Their conditions of occurrence are shown on the Mohr-Coulomb envelope. Modes (I) and (II) are the common failure modes observed, of which Mode (I) is the most critical. Mode (I) is mathematically identified as $\sigma_3<\sigma_t$ and $\sigma_1<0$, while Mode (II) is identified as $\sigma_3<\sigma_t$ and $\sigma_1>0$, and Mode (III) is identified as $\sigma_3>0$ and $\sigma_1>\sigma_{1s}$.

If failure occurs through biaxial extension (Mode (I)), the rock will deform elastically until it fails in a brittle manner. Plastic deformation will not occur. Under this scenario, an elastic analysis is sufficient for evaluating this kind of failure. However, for precise evaluations a strain-dependent yield criterion such as the ones presented by Stacey (1981) or Chang (2006) are desirable, or further still by the strain-softening method described by Hajiabdolmajid et al (2002).

One may insist on pursing plastic analyses using stress-dependent yield criterion such as M-C or H-B. In that case the shear or volumetric strains appear to be the most reliable indicators of realistic failures. Although plastic models are generally thought of not being capable of capturing failures resulting from mechanisms such as biaxial extension (leading to tensile failure) it has, however, been demonstrated here that it can be identified through plastic strain assessments. One reason perhaps is that, since many FEM and FDM codes (including FLAC) are incapable of simulating material failure and fallout, the failed materials simply sit and expand in volume (i.e. dilation). By assessing the volumetric or shear strains, the failed regions can be identified.

5.2 *Significance of tensile strength*

It is now clear that the tensile strength of rock mass is the most critical parameter for the scenario simulated. Many authors (e.g. Diederichs, 2003; Martin et al, 1999; Peli et al, 1991) have shown that the tensile strength can be overly underestimated by the Hoek-Brown criterion for a brittle rock mass under low confinement conditions. These same authors also showed that, in order to obtain strength parameter values that match field observations the value m in the Hoek-Brown criterion must be adjusted – often to unconventionally low values (Diederichs, 2003). Following this argument the value m_i in Table 2 was adjusted, in order to obtain input values that result in observations that match those in the elastic model. With the help of RocLab (Rocscience, 2005) the value of m_i was adjusted until a desired a tensile strength is attained then the corresponding values for c and ϕ were determined. The tensile strength values tested ranged between 0.4 MPa (which is the σ_t in Table 2) and 2.6 MPa (which is the c in Table 2). After random simulations the input values that resulted in observations that matched those in the elastic model were obtained. These are given in Table 5.

Table 5. New input parameters for the standard model.

Parameter	Value
For undamaged rock mass:	
Young's Modulus, E	17.8 GPa
Poisson's ratio, v	0.25
Cohesive strength, c	4.4 MPa
Friction angle, ϕ	51.3°
Tensile strength, σ_t	2.2 MPa
For damaged rock mass:	
Young's Modulus, E_d	12.5 GPa
Poisson's ratio, v_d	0.25
Cohesive strength, c_d	2.4 MPa
Friction angle, ϕ_d	47.2°
Tensile strength, σ_{td}	1.22 MPa

Figure 13 shows the plasticity plot resulting from the new input values. It conforms to the observations in Figure 5. Furthermore, the plastic zone has significantly reduced, to roughly coincide with the region of volumetric straining. Figure 12 shows the shear strain plot resulting from the new input values. The dilated zone has increased but appears to be restricted within the DRZ.

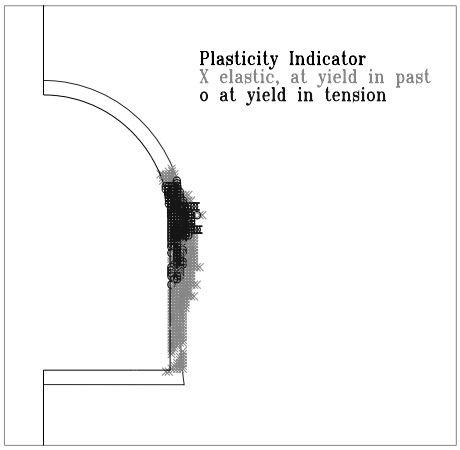

Figure 13. Plastic yielding resulting from the new input values shown in Table 5.

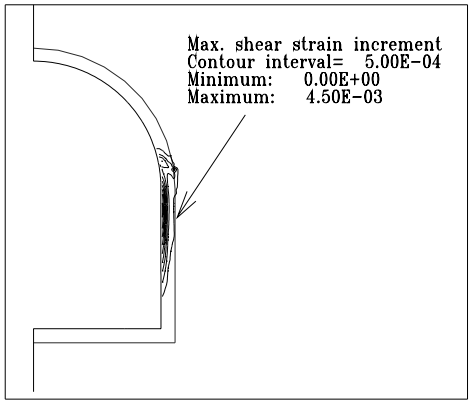

Figure 14. Shear or volumetric strains resulting from new input values shown in Table 5.

5.3 *Effect of damaged rock zone on failure mechanism*

Apparently the models seem to show that the damaged rock zone had no effect on the failure mode. This was evident from the fact that, both of the models, with and without the damaged rock zone, yielded the same results. One reason could be that the main failure mode is purely of extensional type (Mode (I)), which is dependent entirely on the tensile strength of rock mass. Compressive strengths for both rock zones were much higher than the maximum principle stress.

On the other hand, the presence of the damaged rock zone seems to restrict the expansion of the dilated zone. As seen in Figure 14 it is more or less confined within the DRZ. In the base case the depth of the dilated zone was 0.2 m, which is 0.1 m less than the thickness of the damaged rock zone (see Figure 7).

5.4 *Parameter analysis*

Of the parameters tested the variation in the in-situ stresses affected both the tangential stresses and displacement vectors the most (see Figure 8 and 11). The Young's modulus, as an inherent mechanical property of the rock mass, also affected the tangential stresses and displacement vectors quite significantly when varied.

Our classification of the sensitivity of the parameters tested is shown in Table 6. There is no specific criterion for this classification. It is purely based on how much the magnitudes of tangential stresses and displacement vectors vary from the base case observations. The magnitudes of the variation are important in this case. For example, the magnitude of the displacement vectors is in the order of millimeters, which in practical cases will most likely be considered negligible.

Table 6. Classification of parameter sensitivity

Parameter	Sensitivity	
	Tangential stress	displacement
Young's Modulus	High[3]	High
Compressive Strength	Low[1]	Low
Tensile Strength	Low	Low
Thickness of DRZ	Moderate[2]	Low
Overburden thickness	High	Moderate
In-situ stresses	High	High

[1] <20% variation
[2] 10-20% variation
[3] >10% variation

5.5 *Consistency of the observation to practical observations*

Töyrä (2006) modelled three cross-sections of the Arlanda railway (double-track) shuttle station near the city of Stockholm using similar in-situ parameters used in this paper. These cross-sections are shown in Figure 15 with both the designed and final geometries outlined. Töyrä observed that tensile failures were largely occurring in the walls and abutments. The final geometries of cross-sections in Figure 15 also confirmed his observations.

The results from our models appear also to be consistent with the above observations; in particular the volumetric strain plots. The plasticity indicators in Figures 13 and 14, which resulted from the input values in Table 5 appear to conform well to the observations in Figure 15, although in our models we used a single-track tunnel geometry.

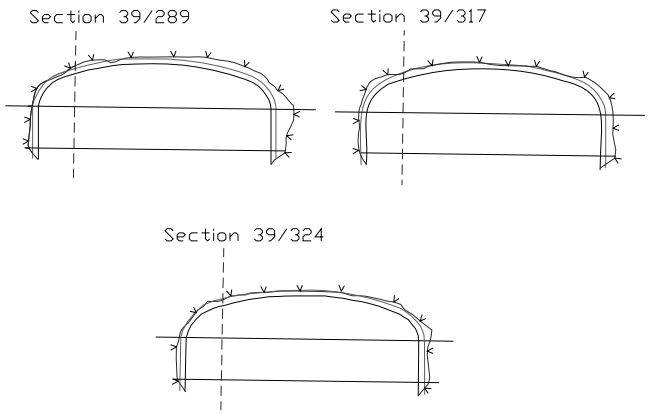

Figure 15. Designed and final geometries of cross-sections, 39/289, 39/317 and 39/324 of the Arlanda Shuttle Station (Töyrä, 2006)

6 CONCLUSION

- Three principle failure mechanisms have been identified: (i) tensile failure due to biaxial extension, (ii) tensile failure from a compressive origin or often

referred to as axial splitting (iii) shear failure from compressive origin.

- Of the three identified failure mechanisms the critical one was the biaxial extension (i.e. when $\sigma_3<\sigma_t$ and $\sigma_1<0$). Under this condition the tensile strength of the rock mass is the most critical parameter. Assuming Mohr-Coulomb or Hoek-Brown criterion appeared to significantly underestimate the tensile strength of the rock mass.
- The development of volumetric strains around the tunnel in the plastic model was seen to be a reliable indicator of failure localities.
- An elastic model was sufficient to indicate potential failure zones. This was be done by evaluating the state of the principle stresses in the elastic model.
- Plastic model using the Mohr-Coulomb resulted in plastic yielding which was not realistic. The simulated results improved dramatically when the tensile strength was adjusted.
- According to the results of the models in this paper the damaged rock zone apparently does not affect the failure mechanisms. However, it does appear to limit the expansion of the dilation zone.

7 REFERENCES

Brady, B.H.G. & Brown, E.T. 1993. *Rock mechanics for underground mining*. Chapman & Hall.

Chang, Y. 2006. Rock strain-strength criterion and its applications. *In Proceedings of the 5th Asian Rock Mechanics Symposium – Rock Mechanics in Underground Construction, Singapore, 8-11 Nov. 2006*, p.331. World Scientific Publishing.

Diederichs, M.S. 2003. Manuel Rocha Medal Recipient Rock Fracture and Collapse Under Low Confinement Conditions. *Rock Mechanics and Rock Engineering, 36(5)*: 339-381.

Diederichs, M.S. 1999. Instability of hard rock masses: The role of tensile damage and relaxation. *PhD Thesis, University of Waterloo*, Waterloo, Ontario, Canada.

Diederichs, M.S. and Kaiser, P.K. 1999. Tensile strength and abutment relaxation as failure control mechanisms in underground excavations. *International Journal of Rock Mechanics and Mining Sciences, 36(1):* 69-96.

Hoek, E., Carranza-Toress, C. & Corkum, B. 2002. Hoek-Brown failure criterion – 2002 edition, *Proc. 5th. North American Rock Mechanics Symposium and 17th Tunneling Association of Canada Conference. ATM-TAC 2002*. University of Toronto, University of Toronto, pp. 267-271.

Hoek, E. & Brown, E.T. 1980. *Underground excavations in rock.* London. Institute of Mining and Metallurgy,

Hoek, E., Kaiser, P.K. & Bawden, W.F. 1995. *Support of underground excavations in hard rock.* A.A. Balkema/Rotterdam/Broofield.

Hajiabdolmajid, V., Kaiser, P.K. and Martin, C.D. 2002. Modelling brittle failure of rock. *International Journal of Rock Mechanics and Mining Sciences, 39(6):* 731-741.

Hajiabdolmajid, V., Kaiser, P. & Martin, C.D. 2003. Mobilised strength components in brittle failure of rock. *Geotechnique, 53(3):* 327-336.

Martin, C.D. 1997. Seventeenth Canadian Geotechnical Cologuium: The effect of cohesion loss and stress path on brittle rock strength. *Canadian Geotechnical Journal, 34(5):* 698-725.

Martin, C.D., Kaiser, P.K., & McCreath, D.R. 1999. Hoek-Brown prameters for predicting the depth of brittle failure around tunnels. *Canadian Geotechnical Journal, 36(1):* 136-151.

Martin, C.D., Read, R.S. and Martino, J.B. 1997. Observations of brittle failure around a circular test tunnel. *International Journal of Rock Mechanics and Mining Sciences, 34(7):* 1065-1073.

Pelli, F., Kaiser, P.K. & Morgenstern, N.R. 1991. Influence of near face behaviour on monitoring of deep tunnels. *Canadian Geotechnical Journal, 28(2):* 226-238.

Priest, S.D. 2005. Determination of Shear Strength and Three-dimensional Yield Strength for the Hoek-Brown Criterion. *Rock Mechanics and Rock Engineering, 38(4):* 299-327.

Read, R.S., Chandler, N.A. & Dzik, E.J. 1998. In-situ strength criteria for tunnel design in highly stressed rock mass. *International Journal of Rock Mechanics and Mining Sciences, 35(3):* 261-278.

Rocscience. 2005. RocLab Version 1.0. Available from: http://www.rocscience.com

Saiang, D., & Nordlund, E. 2007. Continuum Analysis of Shallow Tunnels in Brittle Rock with Damaged Rock Zone Around Their Boundaries. Submitted to: Rock Mechanics and Rock Engineering.

Saiang, D., & Nordlund, E. 2006. A parameter study of the damaged rock zone around shallow tunnels in brittle rock. In C.F. Leung & Y.X. Zhou (eds), *Rock Mechanics in Underground Construction, Proceedings of the 5th Asian Rock Mechanics Symposium, Singapore, 8-11 Nov. 2006*, p.140, World Scientific Publishing.

Stephansson, O. 1993. Rock stress in the Fennoscandian shield. In: J.A. Hudson (Editor), *Comprehensive Rock Engineering*. Pergamon Press, pp. 445-459.

Stacey, T.R. 1981. A simple extension strain criterion for fracture of brittle rock. *International Journal of Rock Mechanics and Mining Science & Geomechanics Abstracts, 18(6):* 469-474.

Töyrä, J. 2006. Behaviour and stability of shallow underground constructions, *Licentiate Thesis*, Luleå University of Technology, Luleå, Sweden.

Analytical solution of displacement for circular tunnel using strain strength criterion

Yanting Chang
WSP Civils, Stockholm, Sweden

ABSTRACT: This paper presents an analytical closed-form elasto-plastic solution for displacement around a circular tunnel. The solution is based on strain-related parameters such as initial strain, strain boundary conditions and a strength criterion in term as strains. Engineering approaches based on such strain-related solutions are advantageous for applications in the so called observational method. This paper will demonstrate that the size of the eventual plastic zone and the strain-related parameters can be estimated directly by evaluations of measured displacements. These parameters are important to evaluate the observed tunnel behaviors compared with the expected behaviors.

1 INTRODUCTION

Displacements are often monitored during rock excavations, not only for monitoring the stability, but also for re-evaluating the design. For instance, displacement monitoring is an essential part of the New Austrian Tunnelling Method (NATM). A design approach known as "the observational method", in which the design is reviewed by measurements during construction, has been adopted in the Eurocodes. When using the observational method, the response time of the instrumentations and the procedures for analysing the results shall be sufficiently rapid in relation to the possible evolution of the construction work. At present, back-calculations based on stress analysis are often performed. But this is a time-consuming procedure.

Sakurai (1981) developed a strain evaluation method to determine the strain distribution in an underground opening directly from the measured displacement. However the method has not been widely used in rock engineering, partially because of lack of a general strength criterion expressed in strains.

In order to utilise the approaches of strain analyses in rock engineering, a general and simple criterion for rock strength in term of strains has been proposed by Chang (2006), based on the compilation of test data from the literature. The strain strength criterion is expressed in term of a linear correlation between the major principal strain and volumetric strain as written as follows:

$$\varepsilon_v = \kappa \cdot \varepsilon_1 - \varepsilon_c \tag{1}$$

where ε_v is the total volumetric strain; ε_1 is the total major principal strain; κ and ε_c are material constants. Under plane strain condition, the strain strength criterion can be translated to the traditional Mohr-Coulomb strength criterion. For engineering purposes, an approach called "strain path analysis" is introduced (Chang, 2006), so that the results of displacement measurements can be easily interpreted and the observed tunnel behaviours can be evaluated.

This paper presents a analytical closed-form solution of tunnel deformation for a circular tunnel subjected to an isotropic initial loading condition. The solution is based on strain-related parameters, such as initial strain, strain strength and strain boundary condition. The work presented in this paper is a part of an attempt to establish a new engineering approach to be used in the observational method for fast and reliable interpretations of field measurements.

2 STRAINS ASSOCIATED WITH TUNNELLING

Before a tunnel excavation, the rock is considered as being constrained by initial strains, denoted by $\{\varepsilon_o\}$. During the course of tunnelling, the strains will be changed from the initial state $\{\varepsilon_o\}$ to a new state $\{\varepsilon\}$ in the strain space. The strain increment due to the tunnel excavation, denoted by $\{\Delta\varepsilon\}$, can thus be written as

$$\{\Delta\varepsilon\} = \{\varepsilon\} - \{\varepsilon_o\} \tag{2}$$

For the case to be studied in this paper, it is assumed that at the initial state $\varepsilon_t = \varepsilon_r = \varepsilon_z = \varepsilon_o$; where ε_o is the initial strain; ε_t , ε_r and ε_z is the tangential, radial and longitudinal total strain respectively. It is also assumed that $\Delta\varepsilon_z = 0$ during tunnel excavation. Equation 2 can thus be explicitly written as follows for an axi-symmetrical problem:

$$\Delta\varepsilon_t = \varepsilon_t - \varepsilon_o \quad \text{and} \quad \Delta\varepsilon_r = \varepsilon_r - \varepsilon_o \tag{3}$$

where $\Delta\varepsilon_t$, $\Delta\varepsilon_r$ is the tangential respective radial incremental strain due to the tunnel excavation. The relationship between the incremental strains and displacement is expressed by the following compatibility equations:

$$\Delta\varepsilon_t = \frac{u}{r} \quad \text{and} \tag{4}$$

$$\Delta\varepsilon_r = \frac{du}{dr} \tag{5}$$

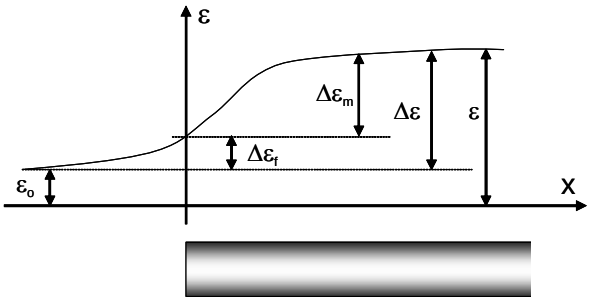

Keys:
ε_o – initial strain

$\Delta\varepsilon$ – tunnel induced total incremental strain

$\Delta\varepsilon_f$ – tunnel induced incremental strain at tunnel face

$\Delta\varepsilon_m$ – measurable tunnel induced incremental strain

ε – total strain

Figure 1. Strains associated with tunnel excavation

where u is the radial displacement caused merely by tunnel excavation; and r is the radial coordinate measured from the tunnel centre. The corresponding incremental volumetric strain is expressed as

$$\Delta\varepsilon_v = \Delta\varepsilon_t + \Delta\varepsilon_r \,. \tag{6}$$

It is well known that rock starts to deform already in front of the tunnel face, as illustrated in Figure 1. At the face, the tunnel has reached about 30% of its final deformation. The tunnel reaches its final deformation within a distance of about 2-5 tunnel radius, depending upon whether the rock is in yielding condition or not. It is obvious that it is not practical to measure the total strain increment $\Delta\varepsilon$ caused by tunnel excavations. Only the strains behind the tunnel face, denoted by $\Delta\varepsilon_m$ in Figure 1, are normally measured in engineering practice.

Based on analyses of test data Chang (2006) has pointed out that under triaxial loading the rock exhibits volumetric contraction i.e $d\varepsilon_v / d\varepsilon_1 > 0$ under elastic condition; whereas rock exhibits plastic behaviour with volumetric expansion i.e. $d\varepsilon_v / d\varepsilon_1 < 0$ when the strains reach the strain yielding surface defined by equation 1. This is an important statement, by which the extents of yielding zone around a tunnel can be detected by measuring the changes of the strains. Since strains have the differential relations with displacements as shown in equations 4 and 5, the strain changes can be estimated from the measured displacements.

3 BOUNDARY CONDITIONS

Generally speaking, a boundary value problem can be divided into "stress boundary value problem" or "displacement boundary value problem", as illustrated in Figure 2. When stresses on all boundaries are specified, the problem is classified as a "stress boundary value problem"; whereas if the displacements or strains on all boundaries are specified, the problem is classified as a "displacement boundary value problem".

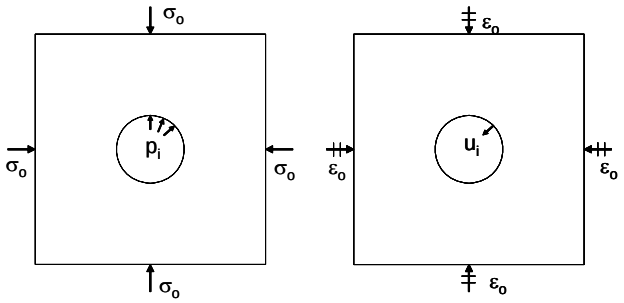

a) stress boundary value problem

b) displacement boundary value problem

Figure 2. Illustration of stress and displacement boundary value problems for isotropic loading condition

For instance, a fictitious pressure p_i is introduced to account the supporting effects of the tunnel face in the traditional "Ground-Reaction-Curve" approach. In this case the initial stress σ_o and the internal pressure p_i on the tunnel wall are specified. Therefore it is a "stress boundary value problem".

For the cases where the displacement at tunnel wall is known by measurements, the problem can be treated as a "displacement boundary value problem". To obtain solutions for such displacement boundary problems, strain-related parameters are preferred.

For a circular tunnel of radius a under isotropic loading, these two types of boundary value problems can be expressed as follows:

- Stress boundary conditions

$$\sigma_r\big|_{r=a} = p_i \quad ; \quad \sigma_r\big|_{r=\infty} = \sigma_o \tag{7}$$

- Displacement boundary conditions

$$u\big|_{r=a} = u_i \quad ; \quad u\big|_{r=\infty} = 0 \tag{8}$$

where r is the radial coordinate; σ_r is the radial stress; u is displacement caused by tunnel excavations; and u_i is the displacement at tunnel wall. The inwards displacement is defined as positive.

Generally speaking, models with stress boundary conditions are suitable for prediction of tunnel behaviours, whereas it is much more advantageous, as it will be shown in this paper, to use such strain-based solutions for analysing observed tunnel behaviours.

The following sections present an analytical elasto-plastic solution for the displacement boundary condition as specified in equation 8 for a circular tunnel subjected to an isotropic loading. The plane strain condition is assumed and the strain strength criterion expressed in equation 1 is used.

4 SOLUTION FOR ELASTIC CONDITION

The solution of the elastic displacement of a circular tunnel caused by tunnel excavations is often expressed as:

$$u = \frac{(1+\mu)}{E}(\sigma_o - p_i)\frac{a^2}{r} \tag{9}$$

where E is elastic modulus; and μ is Poisson's ratio. For the displacement boundary condition expressed in equation 8, where u_i is known, the strain distributions are derived as follows.

From equation 9 the displacement at tunnel wall u_i can be obtained as

$$u_i = \frac{(1+\mu)}{E}(\sigma_o - p_i)\cdot a \tag{10}$$

Eliminating $(\sigma_o - p_i)$ from equations 9 and 10 will lead to

$$u = \frac{u_i}{a}\cdot\frac{a^2}{r} \tag{11}$$

which will give the following distributions of the incremental strains by using the compatibility equations 4 and 5:

$$\Delta\varepsilon_t = \frac{u_i}{a}\cdot\left(\frac{a}{r}\right)^2; \tag{12}$$

$$\Delta\varepsilon_r = -\frac{u_i}{a}\cdot\left(\frac{a}{r}\right)^2 \tag{13}$$

The total strains are thus expressed as follows.

$$\varepsilon_t = \Delta\varepsilon_t + \varepsilon_o = \frac{u_i}{a}\cdot\left(\frac{a}{r}\right)^2 + \varepsilon_o \tag{14}$$

$$\varepsilon_r = \Delta\varepsilon_r + \varepsilon_o = -\frac{u_i}{a}\cdot\left(\frac{a}{r}\right)^2 + \varepsilon_o \tag{15}$$

It is interesting to note that equations 12 to 15 lead to

$$\Delta\varepsilon_v = \Delta\varepsilon_t + \Delta\varepsilon_r + \Delta\varepsilon_z = 0 \quad \text{and} \tag{16}$$

$$\varepsilon_v = \varepsilon_t + \varepsilon_r + \varepsilon_z = 3\varepsilon_o \tag{17}$$

where ε_v is the total volumetric strain during tunnel excavation. Equation 16 and 17 show that under elastic condition, tunnel excavations will not affect the volumetric strain, i.e. the volumetric strain remains constant for a circular tunnel subjected to an isotropic loading.

Under plane strain condition, the initial strain is related to the initial stress by the following relation

$$\varepsilon_o = \frac{(1+\mu)(1-2\mu)}{E}\cdot\sigma_o \tag{18}$$

By using this relation and letting $p_i = 0$ in equation 10, the following equation will be derived:

$$\frac{u_i}{a} = \frac{\varepsilon_o}{1-2\mu} \tag{19}$$

which shows that the final tunnel displacement for an unsupported tunnel can be obtained directly from the initial strain, without knowing the E-modulus.

5 SOLUTION FOR ELASTO-PLASTIC CONDITION

When the total volumetric strain ε_v and the major principal strain ε_t satisfy the strain strength criterion as expressed by equation 1, the rock will undergo plastic deformations. Denoting $\Delta\varepsilon_t^{\,c}$ as the critical strain at which the plastic strain will take place, equation 1 together with equations 3 and 17 will lead to

$$\Delta\varepsilon_t^{\,c} = \frac{(3-\kappa)\cdot\varepsilon_o + \varepsilon_c}{\kappa} \tag{20}$$

Please note that the definition of $\Delta\varepsilon_t^{\,c}$ accounts only for the strains caused by tunnel excavation. In other words, if the excavation induced deformation $\Delta\varepsilon_t = u_i/a$ is larger than $\Delta\varepsilon_t^{\,c}$, a region with plastic deformation will exist.

Within the plastic region, the strain increments caused by tunnel excavation will consist of elastic and plastic components. The compatibility condition will consequently be written as

$$\Delta\varepsilon_t = \Delta\varepsilon_t^e + \Delta\varepsilon_t^p = \frac{u}{r} \tag{21}$$

$$\Delta\varepsilon_r = \Delta\varepsilon_r^e + \Delta\varepsilon_r^p = \frac{du}{dr} \tag{22}$$

where $\Delta\varepsilon_t^e$ and $\Delta\varepsilon_t^p$ are the tangential elastic respective plastic incremental strain; $\Delta\varepsilon_r^e$ and $\Delta\varepsilon_r^p$ are the radial incremental strains. It is well acknowledged that the relationship between the plastic strains can be expressed by $\Delta\varepsilon_r^p = -f\cdot\Delta\varepsilon_t^p$ considering the dilatancy of the rock described by the dilatancy factor f. By using this relationship, the plastic strains can be eliminated from equation 21 and 22, which will lead to:

$$\frac{du}{dr} + f\cdot\frac{u}{r} = \Delta\varepsilon_r^e + f\cdot\Delta\varepsilon_t^e \tag{23}$$

Assuming the elastic strains are constant in the plastic region and have the same value at the boundary between the elastic and plastic region, i.e.

$$\Delta\varepsilon_t^e = -\Delta\varepsilon_r^e = \Delta\varepsilon_t^{\,c} \tag{24}$$

the following solution to equation 23 will be derived by using the displacement boundary condition expressed in equation 8:

$$\frac{u}{r} = \frac{u_i}{a}\cdot\left(\frac{a}{r}\right)^{f+1} + \Delta\varepsilon_t^{\,c}\cdot\frac{f-1}{f+1}\left[1-\left(\frac{a}{r}\right)^{f+1}\right] \tag{25}$$

As it is mentioned that tunnelling is a successive process, it is more advantageous to use formulations for incremental displacement. Denoting du_i and du as the displacement increments due to one excavation step, the following relation between du_i and du is derived from equation 25:

$$\frac{du}{r} = \frac{du_i}{a}\cdot\left(\frac{a}{r}\right)^{f+1} \tag{26}$$

By using the compatibility condition as expressed in equations 4 and 5, the corresponding strain increments caused by this excavation step will obtained as

$$d\varepsilon_t = \frac{du_i}{a}\cdot\left(\frac{a}{r}\right)^{f+1}; \quad d\varepsilon_r = -f\cdot\frac{du_i}{a}\cdot\left(\frac{a}{r}\right)^{f+1} \text{ and} \tag{27}$$

$$d\varepsilon_v = (1-f)\cdot\frac{du_i}{a}\cdot\left(\frac{a}{r}\right)^{f+1} \tag{28}$$

To determine the radius of the plastic region r_p, the boundary condition

$$u/r\big|_{r=r_p} = \Delta\varepsilon_t^{\,c}$$

and equation 25 will give the following expression of r_p :

$$\frac{r_p}{a}=\left(\frac{u_i}{a}\cdot\frac{1}{\Delta\varepsilon_t^{\,c}}\cdot\frac{f+1}{2}-\frac{(f-1)}{2}\right)^{1/(f+1)} \tag{29}$$

The incremental relations between r_p and u_i will thus be:

$$\left(\frac{r_p}{a}\right)^f\cdot \mathrm{d}r_p=\frac{1}{2\cdot\Delta\varepsilon_t^{\,c}}\cdot \mathrm{d}u_i \tag{30}$$

The above analytical elasto-plastic solution for the axi-symmetric problem is summarized as follows:

- Under elastic condition, the distribution of the tunnel displacement with r is determined by equation 11, when the displacement at tunnel surface u_i is known;
- The volumetric strain under elastic condition remains constant during tunnel excavations;
- When the initial strain ε_o as well as the strain strength parameter κ and ε_c are known, $\Delta\varepsilon_t^{\,c}$ expressed in equation 20 is the critical tangential strain. If the tunnel deformation expressed by u_i/a is larger than the value of $\Delta\varepsilon_t^{\,c}$, a plastic zone will occur around the tunnel;
- The radius of the plastic zone can be determined by equation 29 when u_i/r_i and $\Delta\varepsilon_t^{\,c}$ are known;

In tunnelling practice, however, it is not practical to measure the total deformation. It is more advantageous to use the incremental relations such as equations 26 – 28 and equation 30. The following section will give a short description for practical applications of the above solution.

6 APPROACH FOR APPLICATIONS

Propose that displacement measurement by extensometer arranged as shown in Figure 3 has been performed and the displacement increment du caused by the latest excavation has been registered. By curve fitting of the measured displacement, the distribution of du with r, denoted as $\delta(r)$, can be defined. The corresponding strain increments for this excavation step can be determined as follows:

$$d\varepsilon_t=\frac{\delta(r)}{r}\ ;\ d\varepsilon_r=\frac{\mathrm{d}\delta(r)}{\mathrm{d}r}\ \text{and}\ \ d\varepsilon_v=\frac{\delta(r)}{r}+\frac{\mathrm{d}\delta(r)}{\mathrm{d}r} \tag{31}$$

For the region where $d\varepsilon_v/d\varepsilon_t \geq 0$, the rock mass is under elastic condition; whereas if $d\varepsilon_v/d\varepsilon_t < 0$, the rock is having plastic behaviour. The border between the elastic and plastic regions determines the size of the plastic zone r_p. The increment of r_p can be obtained by comparing the current and previous r_p.

The dilatancy factor f can be determined by using equations 27 and 28 as follows:

$$f=1-\frac{d\varepsilon_v}{d\varepsilon_t} \tag{32}$$

When du_i, dr_p, r_p and f are known, the critical strain $\Delta\varepsilon_t^{\,c}$ can be determined by using equation 30, i.e.

$$\Delta\varepsilon_t^{\,c}=\frac{1}{2}\cdot\left(\frac{a}{r_p}\right)^f\cdot\frac{\mathrm{d}u_i}{\mathrm{d}r_p} \tag{33}$$

These estimated values of r_p , f and $\Delta\varepsilon_t^{\,c}$ can be compared with the expected values from the design phase and engineering judgments can then be made.

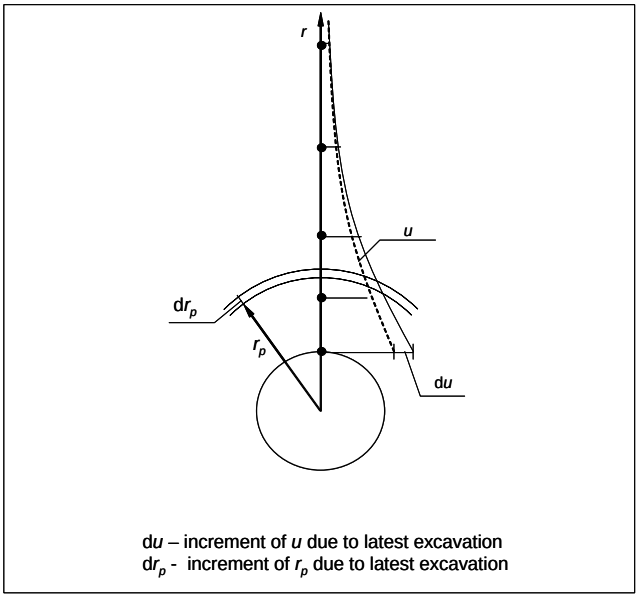

Figure 3. Displacement measurement using extensometer

7 CONCLUSIONS

This paper presents an analytical elasto-plastic solution of strains for a circular tunnel subjected to an isotropic loading. The engineering approach based on the strain-related solution is more advantageous because it is much more straightforward to estimate these strain-related parameters directly by measurements during tunnel excavations. It is shown that by displacement measurement the volumetric strain, the size of the eventual plastic zone and the strain-related parameters f and $\Delta\varepsilon_t^{\,c}$ can be estimated. These parameters are important to evaluate the observed tunnel behaviours. This approach is especially beneficial for the so called observational method, where measurement is an essential part of the design process to verify expected tunnel behaviours.

REFERENCES

Chang, Y. 2006. Criterion for Rock Strain Strength and Its Application. *Proc. 4th Asian Rock Mechanics Symposium, 8-10 November, Singapore.*

Hoek, E. & Marinos, P. 2000. Predicting Squeeze – Part 2: Estimating Tunnel Squeezing Problems. *Tunnels and Tunnelling International, Dec 2000 : 34-36.*

Sakurai, S. 1981. Direct Strain Evaluation Technique in Construction of Underground Opening. *Proc. 22nd U. S. Sympo. Rock Mech, MIT Cambridge, Mass, 278~282. July 1981.*

Stille, H. & Nord, G. 1990. Rock Mechanics. *Compendium, the Royal Institute of Technology, Stockholm, Sweden.*

Numerical analyses of shotcrete reinforcement

F. Perman & J. Sjöberg
Vattenfall Power Consultant AB, Luleå, Sweden

O. Olofsson
Banverket, Borlänge, Sweden

L. Rosengren
Rosengren Bergkonsult AB, Falun, Sweden

ABSTRACT: The work presented in this paper was aimed at increasing the understanding of how to model and evaluate the behavior of shotcrete in numerical models. A parametric study was conducted using two- and three-dimensional continuum models. When simulating the shotcrete in a three-dimensional model, tensile stresses oriented parallel to the tunnel axis developed in the shotcrete, which may cause local cracking. This phenomenon is mostly pronounced when shotcrete is applied close to the tunnel face, and for thin shotcrete layers. A three-dimensional model is required to fully assess the effects of the advancing tunnel face. However, the consequences of exceeding the tensile strength locally may not be critical. The extent of acceptable local overstressing must be judged based on geology, uncertainties, assumptions and simplifications, and previous experiences. It may also be more cost-efficient to remedy local problems as they occur (e.g., by post-sealing) than to change the entire reinforcement design.

1 INTRODUCTION

Presently, massive investments in infrastructure (railroad and road) rock tunnels are planned in Sweden. For railroads, new underground infrastructures (tunnels and stations) in the amount of approximately 4 billion euro are planned under the direction of Banverket, (the Swedish National Railroad Administration) for the next decade. Many of these tunnels will be constructed in urban environments and will be of relatively high complexity, which will necessitate stringent, robust, and reliable design procedures.

The design of the load-bearing structure of rock tunnels is associated with uncertainties, which must be handled in the design process. The national standard for railroad tunnels, *BV Tunnel*, published by Banverket (2005), prescribes that the design of the load-bearing structure should be verified, first through calculations, and later through observations and monitoring during the construction stage.

Verification of the design of shotcrete rock reinforcement for rock tunnels can be conducted using numerical analysis. Recent design work conducted for a tunneling project in Sweden revealed large differences in the calculated loads of the shotcrete between two- and three-dimensional numerical models. The results indicated that high tensile stresses developed in the shotcrete when simulated in a three-dimensional model (Sjöberg et al. 2006). This behavior warranted further investigation to better understand the function of shotcrete rock reinforcement function in numerical models.

The objective of this work was to increase the understanding of shotcrete behavior in numerical models. An additional objective was to propose guidelines for realistic simulation of shotcrete, as well as for evaluation of shotcrete reinforcement function with respect to both load-carrying capacity and durability of a rock tunnel.

2 APPROACH

This study comprised two- (2D) and three-dimensional (3D) continuum numerical analysis, using the finite difference programs *FLAC* (Itasca 2001) and *FLAC^{3D}* (Itasca 2004). The analyses were conducted as a parametric study.

The impacts of different factors were analyzed using a Base Case and then by varying different parameters. The parameters that were varied were: (i) distance between installed shotcrete and tunnel face; (ii) thickness of the shotcrete; (iii) stiffness and strength growth due to curing of the shotcrete; (iv) orientation of the maximum horizontal virgin stress; (v) strength and deformation properties of the rock mass; and (vi) constitutive model for the shotcrete.

3 MODEL DESCRIPTION

3.1 *Model setup*

A typical tunnel geometry for a railroad tunnel in Sweden was chosen for the analysis (Banverket 2005), see Figure 1. In this study the rock cover was set to 5 m.

The model size, for the 3D-model, was chosen to be 200 x 60 x 40 m (length x width x height), see Figure 2. The zone size near the tunnel was 0.5 m and a zone size of 1 m was used far away from the tunnel. At both ends of the central portion of the tunnel a section of 50 meters (with maximum zone sizes of 2 m) were added to minimize the boundary effects. The 2D-model was constructed for a vertical cross-section through the center of the tunnel. To increase precision, a radial mesh was used in the 2D-model. For both the 2D- and the 3D-models, half-symmetric models (symmetry plane along the tunnel axis) were used.

Roller boundary conditions were used on the vertical and bottom boundary of the models, whereas the top boundary

(rock surface) was simulated as a free surface. Similar to earlier work (Sjöberg et al. 2006), a virgin rock stress state according to Equations 1 through 3 was used. This is based on overcoring stress measurements in the Stockholm City area.

$$\sigma_H = -4.5 - 0.075z \quad (1)$$

$$\sigma_h = -3.0 - 0.0375z \quad (2)$$

$$\sigma_v = -0.0027z \quad (3)$$

In these Equations, σ_H and σ_h are the maximum and minimum horizontal stress, respectively, σ_v is the vertical stress (all in MPa), and z is the depth below the ground surface (m). Compressive stresses are here defined as negative. For the Base Case the trend of the maximum horizontal stress was oriented perpendicular to the tunnel axis.

When running the 3D-model, the model was first brought to equilibrium (with stresses and boundary conditions applied). Then, the first 50 m of the tunnel was excavated with no reinforcement installed. The tunnel was then excavated and reinforced in increments of 5 m (corresponding to one blast round), see Figure 2. Finally, the remaining 50 m of the tunnel was excavated with no reinforcement installed. In the 2D-model, the reinforcement was installed after a prescribed amount of deformation in the model, thus simulating the advancing tunnel face.

3.2 *Rock mass properties*

The analysis was conducted using a linear-elastic perfectly-plastic constitutive model with a linear Mohr-Coulomb yield criterion. The rock mass properties were chosen to represent a typical crystalline rock in Scandinavia of fair quality. The resulting values are shown in Table 1.

Each excavation stage was performed in two steps. Excavation was first conducted using high rock mass strength values (to inhibit any yielding). The material strength was then reduced to their correct values and the model allowed to come to a final equilibrium state.

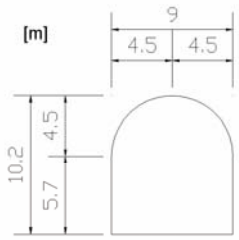

Figure 1. Tunnel geometry.

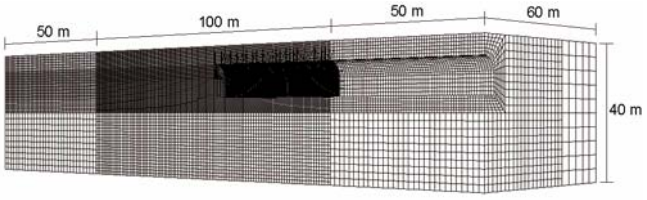

Figure 2. Geometry of the 3D-model, showing excavation of half the tunnel length with reinforcement installed.

This procedure was employed to minimize inertial effects, due to sudden excavation of rock, which can lead to unrealistically large yielding in the models.

3.3 *Reinforcement properties*

A typical reinforcement with systematic rock bolting and fiber-reinforced shotcrete was used. The properties for the reinforcement are shown in Table 2 and Table 3. In the 3D-models, the shotcrete was simulated as a linear-elastic shell element since no plastic material model is available for this type of structural element in *FLAC*^{3D}. In the 2D-analysis using *FLAC*, both a linear-elastic, and an elasto-plastic beam element was used. The reinforcement was installed in the roof and walls down to the tunnel floor.

3.4 *Parametric study*

The parameters that were varied are presented in Table 4 and in more detail below. In Case 3 the shotcrete curing process was simulated by stiffness and strength growth with time, as shown in Figure 3. This process was simulated by changing the Young's modulus for the shotcrete in each section to values of 1, 11, 14, and 16 GPa, corresponding to a distance from the tunnel face of 0, 5, 10, and 70 m, respectively (assuming one blast round every second day).

In Case 5 the strength and deformation properties of the rock mass was set to lower values: E_m = 12.6 GPa, c_m = 1.46 MPa, ϕ_m = 57.5º, and σ_{tm} = 0.14 MPa. For Case 6 only a 2D-analysis was conducted with a plastic constitutive model for the shotcrete. Two different cases where tested, with elasto-plastic material model and also with curing of the shotcrete. The curing of the shotcrete was simulated as in Case 3, but also with change in compressive strength (f_{cck} = 0.3, 16.3, 24.4, 30.5 MPa) and tensile bending strength (f_{flcrk} = 0.2, 2.6, 3.5, 4 MPa), see Figure 3.

Table 1. Rock properties for the Base case.

Parameter	Value
Young's modulus (E_m)	15.2 GPa
Poisson's ratio (ν_m)	0.25
Bulk modulus (K_m)	10.1 GPa *
Shear modulus (G_m)	6.1 GPa *
Density (ρ_m)	2800 kg/m^3
Cohesion (c_m)	2.16 MPa
Friction angle (inner) (ϕ_m)	61.9º
Tensile strength (σ_{tm})	0.26 MPa
Dilation angle (ψ_m)	0º

* calculated from ν_m and E_m

Table 2. Rock bolt parameters for the Base case.

Parameter	Value
Bolt length (l)	4.0 m
Bolt distance (c/c)	2 m
Diameter (D)	0.025 m
Young's modulus (E_b)	200 GPa
Poisson's ratio (ν_b)	0.25
Density (ρ_b)	7800 kg/m^3
Tensile strength (F_{yk})	246 kN
Tensile failure strain (ε_g)	5 %
Shear coupling spring stiffness (K_s)	9.62 GN/m/m
Normal coupling spring stiffness (K_n)	9.62 GN/m/m
Shear coupling spring cohesion (S_s)	707 kN/m
Normal coupling spring cohesion (S_n)	707 kN/m

Table 3. Shotcrete parameters for the Base case.

Parameter	Value
Young's modulus (E_s)	16 GPa
Poisson's ratio (ν_s)	0.25
Density (ρ_s)	2300 kg/m^3
Compressive strength (f_{cck})	30.5 MPa
Tensile bending strength (f_{flcrk})	4 MPa
Thickness (t_s)	0.05 m

Table 4. Parameters that were varied compared to the Base case.

Case	Changed parameters (Base case value in parentheses)
1a	Distance between shotcrete and tunnel face is 5 m (0 m).
1b	Distance between shotcrete and tunnel face is 10 m (0 m).
2	Thickness of the shotcrete is 0.15 m (0.05 m).
3	Stiffness and strength growth due to curing of the shotcrete.
4	Orientation of the maximum horizontal virgin stress is along the tunnel axis (perpendicular).
5	Strength and deformation properties of the rock mass is set to lower values.
6a	Material model for the shotcrete is plastic.
6b	Material model for the shotcrete is plastic, and shotcrete curing is simulated.

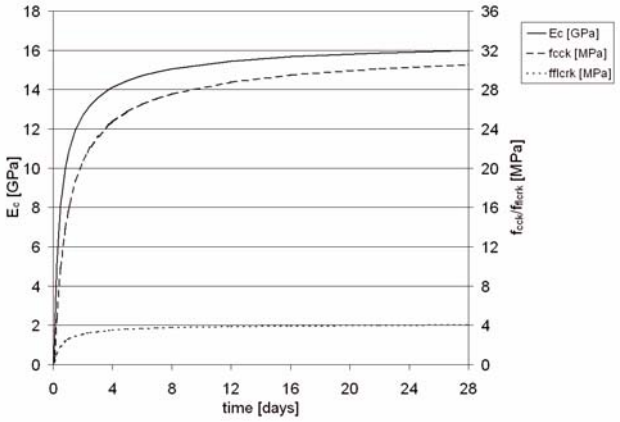

Figure 3. The growth in stiffness (E_c), compressive strength (f_{cck}), and tensile bending strength (f_{flcrk}) for shotcrete during curing.

4 RESULTS

4.1 *Evaluation methodology*

The results from the parametric study were evaluated especially with respect to induced outer-fiber stress in the shotcrete, which was compared with the shotcrete strength for compression and tension. The outer-fiber stresses in the shotcrete for the 3D-models were extracted directly from *FLAC*^{3D}. The outer-fiber stress for the 2D-models in *FLAC* cannot be extracted directly from the code; rather, they have to be calculated using Navier's formula.

The outer-fiber stress calculated in the 3D-models was presented as contours on the tunnel surface (i.e. for the shotcrete elements). These plots were "unfolded" to show the entire tunnel section, from roof through spring line and floor. Furthermore, histograms showing the distribution of calculated minimum stress in the shotcrete were presented.

All models reached equilibrium and are showing stable condition. This means that the large-scale stability is satisfactory for all cases.

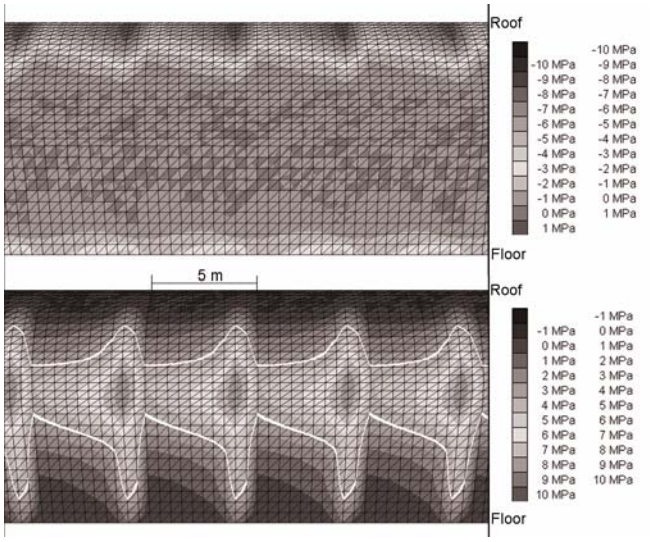

Figure 4. Calculated major and minor principal stress in the outer-fiber of the shotcrete along the tunnel for the Base case. In the lower figure lines with 4 MPa tensile stress is marked in white.

4.2 *Base case*

Calculated major and minor principal stress in the outer-fiber of the shotcrete along the tunnel are shown in Figure 4. A large area around the spring line is exceeding the tensile strength (4 MPa) for the shotcrete. The tensile stress is marked in the figure as white lines. The stress in the shotcrete in one section (of 5 m) is dependent on the distance to the face on installation. This is shown in the figure as a pattern with darker/lighter colors that is repeating itself with an interval of 5 m.

4.3 *Parametric study*

The induced outer-fiber stress did not exceed the compressive strength for any case. However, the results indicated that local overstressing in tension could occur to various extents in the 3D-models. The direction of the maximum tensile stress is generally oriented parallel to the tunnel axis, thus making this a 3D-effect that cannot be simulated using 2D-models.

The calculated minor principal stress in the outer-fiber of the shotcrete along the tunnel for the best and worst cases in the 3D-models, Case 1b and Case 5, are shown in Figure 5. A histogram showing the distribution of calculated minor principal stress in the shotcrete is shown in Figure 6 for the 3D-models: Base Case, Case 1a, and 1b. The percentage of shotcrete elements for which the tensile strength was exceeded for each case is shown in Table 5. For Case 6, in which an elasto-plastic material model was used, the numbers in Table 5 refer to actual tensile failure in the shotcrete.

The results further showed that the distance between installed shotcrete and the tunnel face was the most significant parameter leading to this behavior. This effect of high tensile stresses in the axial direction is judged to be real, although there are no known observations from civil constructions since the shotcrete (traditionally) often is installed far away from the face.

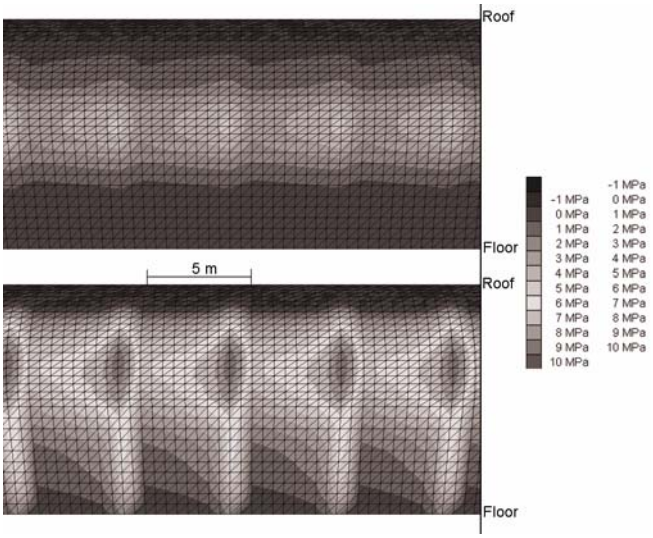

Figure 5. Calculated minor principal stress in the outer-fiber of the shotcrete along the tunnel for the best case, Case 1b (upper) and worst case, Case 5 (lower).

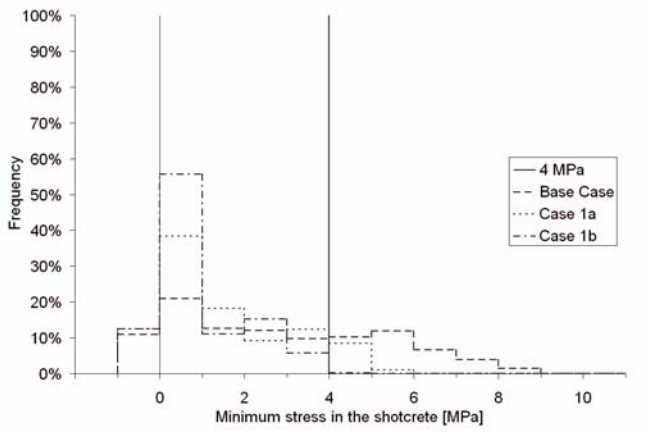

Figure 6. Histogram showing the distribution of calculated minimum stress in the shotcrete for the Base Case, Case 1a, and 1b in the 3D-models.

5 DISCUSSION AND CONCLUSIONS

Based on the findings from the modeling, it can be concluded that the risk for exceeding the tensile strength of the shotcrete is reduced for the cases when: (i) the shotcrete is installed farther from the face; (ii) thicker layer of shotcrete is applied; (iii) shotcrete is simulated with strength growth (due to curing); (iv) the maximum horizontal stress is oriented axial to the tunnel; and (v) higher values of the strength and deformation properties of the rock apply.

In conclusion, it is judged that a 2D-model is sufficient only for analysis of deformation and stability, but not for simulating the effect of an advancing face when the shotcrete is installed close to the face. A 3D-numerical model is required to fully assess the effects of tunnel face advance. It follows that such models should focus on simulating the excavation and reinforcement installation sequence as realistically as possible, in addition to determining realistic and representative values on strength and deformation properties of the rock mass, as well as loading conditions (virgin rock stresses).

When evaluating numerical models with respect to the function of the shotcrete reinforcement, it is suggested that the calculated outer-fiber stress is compared with the compressive and tensile strengths. However, the practical consequences of a predicted local failure of the shotcrete must also be valuated. If the tensile strength is exceeded locally, the stability or the bearing capacity of the whole construction may not necessarily be jeopardized. An assessment of the overall stability must be conducted in parallel with the assessment of each single reinforcement element. For a reinforcement system consisting of interacting rock bolts and shotcrete, a high bearing capacity can be retained even if a portion of the shotcrete or rock bolt is loaded to its peak load. When evaluating the model results, a judgment of the acceptable extent of local overstressing in the shotcrete should be based on geology, uncertainty in input data, assumptions and simplifications made, previous experience, and the future consequences.

Table 5. Results showing to what extent the tensile strength is exceeded in the shotcrete. For Case 6 the extent of tensile failure is shown.

Case	Short description	3D-model	2D-model
Base		34 %	19 %
1a	5 m distance to face	10 %	0 %
1b	10 m distance to face	0 %	0 %
2	0.15 m shotcrete	21 %	10 %
3	Shotcrete curing	19 %	0 %
4	Orientation of σ_H parallel to tunnel	14 %	0 %
5	Low strength on rock properties	46 %	26 %
6a	Plastic shotcrete	N/A	13 %
6b	Plastic shotcrete with curing	N/A	39 %

Finally, the effect of a local overstressing may also be linked to the construction process and the total (life) cost for a tunnel. It may be more cost-efficient to remedy local problems as they occur (e.g., post-sealing tensile cracks in shotcrete by applying additional shotcrete) than to over-design the shotcrete only to cope with local cracking problems. The final verification of rock reinforcement and the capacity of the load-bearing structure must be done during the construction using observations, measurements and follow-up of installed rock reinforcement.

ACKNOWLEDGEMENTS

The work presented in this paper was sponsored by Banverket, which is hereby acknowledged, along with the permission to write and present this paper.

REFERENCES

Banverket. 2005. BV Tunnel. Standard BVS 585.40.

Itasca. 2001. FLAC. Version 4.0. Manual. Minneapolis: ICG.

Itasca. 2004. *FLAC^{3D}*. Version 2.10. Manual. Minneapolis: ICG.

Sjöberg, J., Perman, F., Leander, M. & Saiang, D. 2006. Three-dimensional analysis of tunnel intersections for a train tunnel under Stockholm. In *North American Tunneling 2006. Proc. North Americal Tunneling 2006 Conference, 10–15 June, 2006*: 39–48. London: Taylor & Francis.

Rock erosion in spillway channels — a case study of the Ligga Spillway

L. Mörén
Tyréns AB, Umeå, Sweden (formerly at Vattenfall Power Consultant AB, Luleå, Sweden)

J. Sjöberg
Vattenfall Power Consultant AB, Luleå, Sweden

ABSTRACT:. High flow in spillway channels of hydropower dams may cause erosion of the rock in the channel, which may result in damage of concrete structures, change of flow patterns and/or endanger dam stability. This paper presents a case study of the Ligga spillway, in which physical model tests and dynamic numerical analysis were used to study the potential for erosion for several alternative designs of the spillway channel. The results from the numerical modeling clearly showed that a flattened channel bed (in the upper portion), in combination with a constructed groove in the middle portion, was the most favorable to reduce the amount of rock scour. This design was chosen to be implemented for the re-construction of the spillway channel, which is currently underway.

1 INTRODUCION

The global climate changes will probably result in an increased precipitation in Sweden. This will cause higher floods in the rivers and increased water loads on existing hydropower dams along the rivers. This potential situation will result in higher demands on the safety of the dams, and new guidelines for design flood has been determined by the flood committee appointed by SMHI (the Swedish Meteorological and Hydrological Institute) and the hydropower industry (Flödeskommittén 1990). In order to maintain the safety of the dams, remedial measures and investigations to increase the safety have been undertaken for many of the larger dams in Sweden.

Higher floods in the spillway channels of hydropower dams may cause erosion of the rock in the channels. There are several hydropower stations in Sweden in which the spillway channels have been subjected to extensive rock erosion, even though none of the spillways have experienced any long-term high flow.

This paper focuses on the Ligga spillway in the Luleälven river, where the risk for rock erosion in the current spillway channel is judged to be large. Using physical model tests and numerical analysis, several alternative designs of the channel were investigated, with the aim of reducing rock scour.

2 PROBLEM DESCRIPTION

2.1 *General*

Hydropower is an important energy source and in Sweden alone there are nearly 1900 hydropower plants, and some 190 hydropower dams (Johansson et al. 2003). Many of these dams are filling dams with filling material such as till, silt, gravel and clay. This construction is sensitive to overtopping flow and can easily break if water starts to flow over the top. An important part of the dam construction is therefore spillways with floodgates through which water can be discharged in flood times. The spillway channels are in many cases blasted into the rock mass or located directly in the old river bed.

When water is discharged in a spillway it is often done with a high flow. The load from the flowing water can cause erosion of the rock in the channel, where whole blocks become detached from the rock mass. The blocks that erode can be large, with volumes of up to 20–30 m^3, see Figure 1.

Block erosion in a spillway channel may result in:

- damage of the concrete structures if eroded blocks crashes into them,
- changes in the flow patterns in the channel if the erosion is extensive or if eroded blocks land in impropriate places,
- undermining of guidewalls and other constructions if the rock mass where these are placed erode, and
- stability problems of the dam if the erosion propagates back towards the dam constructions

Figure 1. Eroded block in the spillway channel of the Harsprånget hydropower plant.

2.2 *Mechanism for block erosion*

Rock block erosion due to flowing water is caused by the pressure fluctuation in the water. The pressure varies because of turbulence and waves in the water. The rock mass in a spillway channel is affected by a surface shear force resulting from flowing water passing over the upper surface of the blocks. The rock mass is also affected by varying pressure caused by the turbulence and waves in the water. This varying pressure can cause pressure differences between upper and lower parts of blocks, which may result in instantaneous lift forces.

The combination of lift forces and drag forces from the flowing water can enable entire rock blocks to detach from the rock mass. The extent of the erosion depends on the magnitude of the difference between the shear forces, lift forces and resisting forces, the mass of the rock blocks, and the length of time during which the shear forces exceed the resisting forces (Lorig 2002). The jointing pattern affects the vulnerability of a rock mass to water loads—a rock mass with sub-horizontal jointing is particularly susceptible to block erosion from flowing water. Joints dipping in the direction of the flow also results a higher potential for block erosion (Cato & Mattewson 1990).

3 APPROACH

In the Luleälven and Indalsälven rivers, there are several hydropower stations for which the spillway channels have been subjected to extensive block erosion, e.g. the Satisjaure, Harsprånget, and Midskog stations. The relatively extensive problems prompted re-design of several of the channels. Using physical model tests and numerical analysis, several alternative designs of the channels were investigated, with the aim of reducing rock scour. The channels were then rebuilt based on these results (Billstein et al. 2003, Billstein & Ekström 2004). These remedial measures have later proven to work well when the stations were taken in operation again, proving that the methodology used for assessing rock erosion (physical model tests complemented by numerical analysis) was sound and reasonable (Billstein et al. 2003). Hence, a similar methodology was utilized for the investigation of a new design of the Ligga spillway.

4 THE LIGGA CASE

4.1 *The Ligga spillway conditions*

The Ligga hydropower plant is located in the Stora Luleälven river, 25 km north of the town of Jokkmokk. The dam is classified as a high-risk dam (by the flood committee), which means that it shall be possible to discharge 2000 m^3/s water from the dam reservoir without endangering the safety of the dam. The spillway channel has been subjected to extensive block erosion, despite that the largest documented discharge is only 900 m^3/s. The risk for continued (and increased) rock erosion in the current spillway channel is therefore judged to be very large.

The rock mass in the spillway channel consists mainly of granite. The dominating jointing pattern in the rock mass is subhorizontal joints with small spacing. The joint spacing varies between 0.1–1 m, see also Figure 2.

Figure 2. The spillway channel in Ligga.

4.2 *Erodability index*

The erodablility of a rock mass due to flowing water is difficult to determine due to the complexity of flow and rock conditions. A semi-empirical method exists in which the risk for scour is predicted based on an erodability index. This method is based on 137 field observations on erodability of emergency spillways and presents a threshold relationship between a geomechanical index of the bed materials and the erosive power in the water (Annandale, 1995). When the erodability index is calculated for the rock mass in the Ligga spillway channel and compared with the power in the water for a discharge of 900 m^3/s, a high risk of damaging scour is predicted as shown in Figure 3. In order to improve the dam safety, increase the capacity of the discharge through the floodgates, and still reduce the high risk of scour, the spillway channel has to be redesigned.

4.3 *Numerical analysis*

4.3.1 *Physical model tests and indata*

To determine the amount of the measures that has to be done in the Ligga spillway channel to reduce the risk of scour, physical model tests combined with numerical analysis was performed. In the physical model tests a 1:50 scale model of the spillway channel was built at the Vattenfall laboratory in Älvkarleby. The model was used to identify problem areas and to test different designs for the spillway. Data regarding water depth, pressure fluctuations at specific exposed locations and flow velocities at two different flows and designs of the spillway were registered (Yang et al. 2006). This data were used as input (load from flowing water) in the numerical model. The two examined flows that were used were 900 m^3/s and 2040 m^3/s. A new design of the spillway, in which a groove was created (through blasting) into the middle portion of the channel bed (see Figure 4), gave the most favorable flow pattern in the physical model tests. This design was subsequently investigated in the numerical analysis.

4.3.2 *Numerical method*

Numerical analysis was performed in order to examine if the design judged most favorable from the physical model test also reduces the risk of rock erosion. Dynamic analysis is necessary, because of the varying loads from flowing and turbulent water. The distinct element program *UDEC* (Itasca 2004) was chosen for this type of analysis.

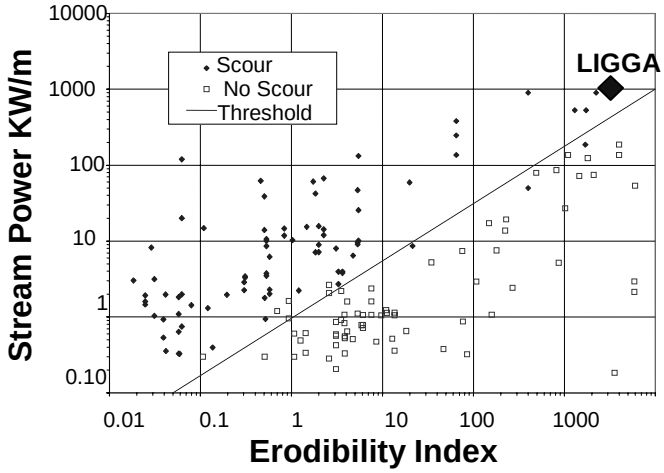

Figure 3. Erosion threshold for rock with the spillway of Ligga marked.

Figure 4. The design of the spillway that gave the most favorable flow pattern in the physical model tests.

The simulated dynamic loading comprised the pressure variations on the rock mass surface due to turbulence in the flowing water. Data of pressure variations was based on the physical model test where the pressure was registered at 3–5 locations in the channel bed. Static loading in the model was due to the static water head and to the shear forces caused by water passing over the upper surface of the rock blocks. The magnitude of the static loading was based on results from measurements in the physical model tests.

Calibration and validation of the numerical model were performed by using loading values for a 900 m^3/s discharge (from the physical model) applied on two profiles of the channel—one profile at the right-hand side of the channel and one profile at the left-hand side of the channel (looking downstream). The right-hand side of the channel has been exposed to more erosion than the left-hand side for the 900 m^3/s flow. The model was thus calibrated, by changing the strength properties of the joints, until model results agreed with actual observations of block erosion.

4.3.3 *Conducted numerical analysis*

Three different profiles of the channel were modeled in the numerical analysis; Two profiles were from the current design and one profile from the new design of the spillway that gave the most favorable flow pattern in the physical model tests. The profiles for the current design were investigated both for calibration (as described above) as well as to examine the effects of maximum discharge, 2040 m^3/s, in the present channel, in terms of risk for erosion. The new design was modeled to examine if the redesigning was an adequate measure to decrease the risk of erosion.

Jointing pattern and rock properties in the model were determined based on field studies in the channel to get the profiles as site-specific as possible. The rock mass was generalized to have two joint sets—one subhorizontal set with 5˚ dip and one vertical joint set.

The sensitivity of the variations in parameters in the models was studied through a parametric study, in which one parameter at the time was varied, and the difference in extent of erosion as predicted by the model was observed. An example of one of the examined profiles with varying loads applied is shown in Figure 5. The erodability of the rock was judged by studying the displacements and separation of rock blocks in the model.

4.4 *Results*

The parametric study showed that the erodability in the model was more affected by the tensile strength than the cohesion of the joints. Furthermore, the joint spacing of the subhorizontal joint set had a large effect on the erosion. A change in the joint spacing of only 10 cm could change the behavior from no erosion to extensive erosion.

For the analysis of the various designs of the Ligga channel, the tensile strength and the cohesion were set to zero as this gave the best agreement with observed behavior. The model of the right-hand side of the channel for the current layout showed that there is a large risk for erosion both for 900 m^3/s and 2040 m^3/s water discharge. The results of the analysis of the left-hand side of the current channel showed no erosion for these conditions.

The numerical analysis of the new design of the channel showed that a discharge of 900 m^3/s caused erosion in the upper portion of the channel In fact, all of the examined cases with this new design indicated a high risk for erosion. This result prompted new physical model tests, which were aimed at reducing the turbulence in the water in the upper portion of the channel. This was achieved by refilling an old erosion damage located below the sluice gates.

New calculations were carried out based on the data from these new physical model tests. These analyses (with a flattened channel bed in the upper portion) showed no erosion for a discharge of 900 m^3/s. Under the action of water loads from the discharge of 2040 m^3/s, some rock erosion developed, but to a lesser extent than for the same flow without the flattened start of the channel bed, compare Figure 6 a) and Figure 6 b).

5 CONCLUSIONS AND RECOMMENDATIONS

The results from the numerical analysis of the Ligga spillway can be summarized as follows:

- The risk for block erosion in a rock mass is strongly related to the joint spacing of subhorizontal joint sets, such as bedding planes or exfoliation, for which a small spacing results in a high risk of erosion.

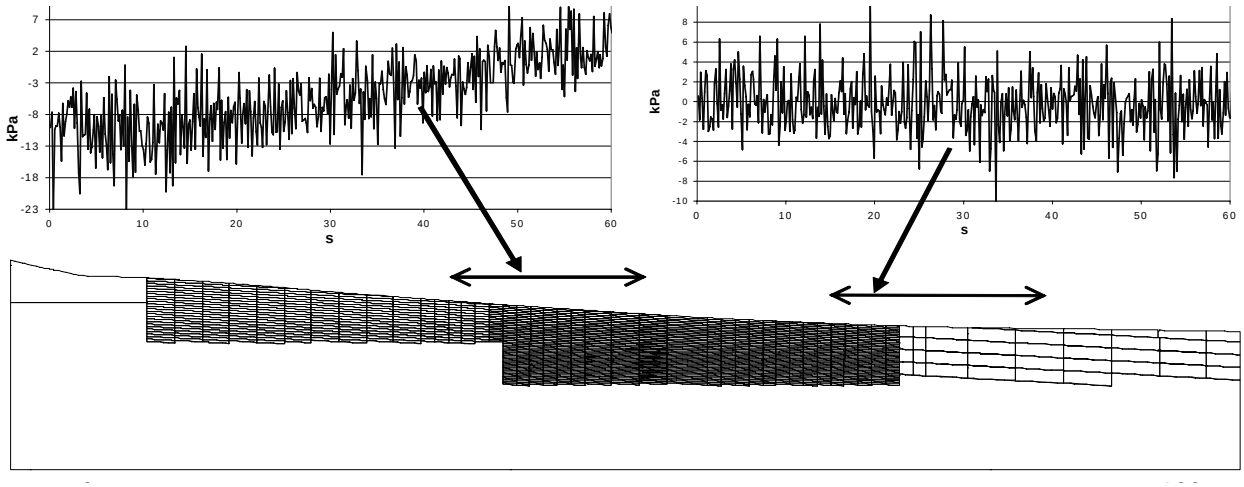

Figure 5. One of the profile used in the numerical model with the applied varying loads applied.

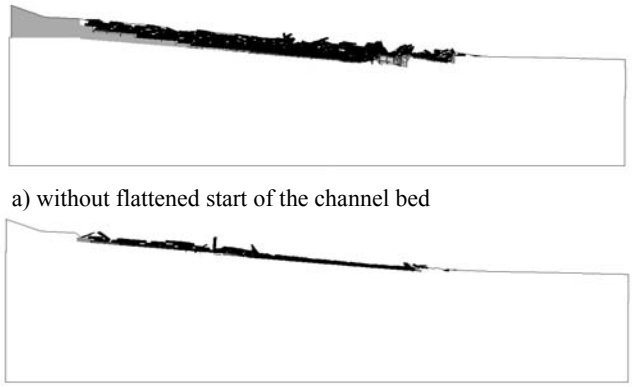

a) without flattened start of the channel bed

b) with flattened start of the channel bed

Figure 6. The black parts show erosion in the redesigned spillway with discharge of 2040 m^3/s water.

- The scatter and amplitude of the pressure variations (due to turbulence and waves in the flowing water) strongly affects the extent of the rock erosion in the channel.
- The design of the Ligga spillway channel, in which a groove was blasted into the middle portion of the channel bed and the upper portion of the channel was flattened, greatly reduced the risk for erosion.

A groove in the middle of the channel in Ligga concentrates the flow and reduces the loads from the water at the edges of the channel. The risk of erosion will therefore decrease at the channel edges, whereas the risk remains large in the middle part of the channel. By lowering the load of water in the right-hand side of the channel the risk of erosion undermining the guidewalls is reduced. A failure of the guidewall could endanger the whole dam. Severe erosion in the middle part of the channel may also cause problems; the flow pattern can change so that the stability of the dam is jeopardized. Hence, it is recommended that the upper portion of the blasted groove is reinforced.

This summer (2007), remedial works are planned for the spillway channel of Ligga. The chosen new design is based on the present study. The layout will be a reinforced groove in the middle portion of the channel and flattening of the channel bed in the upper portion.

ACKNOWLEDGEMENTS

The work presented in this paper was sponsored by Vattenfall AB, Vattenkraft. The permission by all involved project sponsors, in particular Leif Ask, to publish this work is hereby acknowledged.

REFERENCES

Annandale, G.W. 1995. Erodability. *Int. J. Hydraulic Research*, 33: 471-494.

Billstein, M., Carlsson, A., Johansson, N. & Söder, P. E. 2003. Midskog gets Physical…and Numerical, *International Water Power & Dam Construction*, 55: 22-26.

Billstein, M. & Ekström I. 2004. Upgrading of Harsprånget hydropower plant to meet the discharge criteria and increase the dam safety. In *Proc.of the ICOLD 72nd Annual Meeting, Seoul, Korea*.

Cato, K. D. & Mattewson, C. 1990. Rock Material Performance during Emergency Spillway Flows. *Proc. of the 1990 Annual Symp. on Engineering Geology & Geotechnical Engineering, Idaho State university, Pocatello, Idaho*: 29.1-29.15

Flödeskommittén 1990. Riktlinjer för bestämning av dimesionerande flöden för dammanläggningar. Statens Vattenkraftverk, Svenska kraftföreningen, Swedish Meteorological and Hydrological Institute, Stockholm:

Itasca. 2004. *UDEC. Version 4.0*. Manual. Minneapolis: ICG.

Johansson, S., Mill, O., Fridofsson, T. & Hammar, L. 2003. Kompetensförsörjning inom älv- och dammsäkerhet − En behovsstudie av högskoleutbildning och forskning. Report 03:28, webpage: Värmeforsk http://www.svk.se/upload/3556/Kompetensforsorjning_alv_och_dammsakerhet.pdf (2004-11-04).

Lorig, L. 2002. Numerical modeling of Spillway Erosion at Midskog Dam in Sweden. Itasca, Santiago report to SwedPower.

Yang, J., Amnell, G., Skärberg, P. & Aurosell, U. 2006. Ombyggnad av Ligga kraftstation – Modellförsök med dammsäkerhetshöjande åtgärder. Report number U06:01, Vattenfall Utveckling AB, Älvkarleby.

SveBeFo
Box 47047
SE-100 74 Stockholm
Telefon 08-692 22 80 • info@svebefo.se
Besöksadress: Mejerivägen 4
ISSN 1104 - 1773 • SVEBEFO-R--85--SE
tbk.